Technical University Munich and BOKU Vienna

Chair for Biogenic Polymers (TUM) and Institute of Physics and Materials Science (BOKU)

Computational fluid dynamics of a microfluidic cell

Dardan Bajrami

October 29, 2021

Supervisors: Prof. Dr. Cordt Zollfrank (TUM) and Prof. Dr. Helga Lichtenegger (BOKU)

Abstract

The bio-mediated structuring of cellulose excreting microorganisms with microfluidic devices, is a promising new way to create novel materials with hierarchical structures and extraordinary mechanical properties. The understanding of the hydrodynamic phenomena occurring in the microfluidic cell is essential for the uniform distribution of the microbial fluid and therefore the effective assembly of a structured template for further processing into a composite material. This study aims to determine the hydrodynamic characteristics in a microfluidic cell, with computational fluid dynamics, in order to detect geometrical conditions that lead to suboptimal cellulose buildups and additionaly to expand the understanding of the rheotactic behavior of microorganisms in microfluidic cells based on general fluid flow, the occurrence of secondary flows and turbulence in the system.

In this study we performed simulations of fluid flows in microfluidic geometries designed for specific observation approaches and complement them with real bacterial celullose growth experiment analyses, we did find that the geometry leads to uneven fluid flows and insufficient fluid distribution due to design flaws in the inlet and outlet areas. Moreover, we could demonstrate the existence of laminar flows and secondary flows in the system. In addition, the findings could be used for the analysis of the formation of biostreamer and bacterial cellulose in the chamber area. The results indicate that the formation of primary biostreamers in microfluidic cells probably results from the formation of secondary flows and the viscoelastic response of the microorganisms to the fluid flow.

Acknowledgements

I would first like to thank Moritz Klotz for the close cooperation, advising me through this thesis, always providing valuable guidance throughout this project and the constant willingness to help. Also i would like to thank Bernhard Huber for the willingness to assist me with all CFD problems.

I would like to thank Prof. Dr. Cordt Zollfrank for allowing me to conduct this research in his lab during these special times and for his exciting lectures, which motivated me to start the thesis in the Chair for Biogenic Polymers. Also i would like to tank Prof. Dr. Helga Lichtenegger for her willingness to take over the co-supervisorship and her inspiring bionics lecture in Vienna.

My thanks goes to Anna-Sofia, Alex, Thore und Abishek for their kind support and company during my time in Straubing and to Julien and Jan to their friendship and support here in Basel.

I especially want to thank Qendresa, who was always there for me during this time, whether study-related or private and who shows me every day a little bit more of myself.

Finally, I would like to thank my family and especially my brother for their loving support and their infinite patience.

I am very grateful for the time I have spent at TUM and BOKU and want to thank again everyone who made this rather unusual path possible.

Contents

List of Figures

List of Tables

Chapter 1

Introduction

1.1 Outline

Natural materials such as bone, nacre or teeth show extraordinary mechanical properties, such as high toughness or strength. The fundamental reason for this is the nano- and micro-scale composite hierarchical material structure that the materials exhibit. In order to use such outstanding properties e.g. in medicine and to transfer them to artificial materials, microfluidic cells are intended to serve as a leading structure, to create bio-mediated templates for composite material production. For this purpose, extracellular polymeric substances (EPS) forming microorganisms are introduced into the microfluidic cell to create a structured template of EPS by regulating the rheotaxis of the microorganisms. EPS are natural polymers of high molecular weight secreted by microorganisms into their environment. The two key mechanisms of the successful structure formation are the creation of an optimal geometry for the bacterial fluid distribution in the microfluidic cell and the understanding of the rheotactic mechanisms of the microorganisms inside fluid flow. The difficulty is that these mechanisms are difficult to study experimentally and therefore other research methods must often be used. Computational fluid dynamics has been proven to be a successful method to analyze hydrodynamic problems in complex geometries such as the microfluidic cell is. The simulation of the fluid flow of the geometry, can simply simulate hard-to-study processes and detect unrecognized geometric errors. In addition, a general understanding of fluid flow and rheotactic processes of microorganisms can be identified and described. The findings can be used to improve fluid flow and the structuring of EPS in the microfluidic cell.

1.2 Biofilm and EPS formation and its relevance

The formation of hierarchically structured materials in microfluidic cells requires a uniform distribution of directional layer structure of the extracellular polymeric substances secreted by the biofilm. To understand the processes that occur in the microfluidic cell an introduction to the biological processes will be given in the next sections.

1.2.1 Introduction to biofilms

Microorganisms form polymicrobial agglomerations of various strains on surfaces, contrary to the belief, that microorganisms occur only as individual pure organisms. These agglomerations can take the form of films, mats, flocs, sludges and are usually called biofilms.(Flemming and Wingender, 2010) The agglomeration serves the microorganisms to better counteract external effects such as shear forces, antimicrobials or the immune system, but also to promote mutual growth with the exchange of substrate or metabolic products (Vasudevan, 2014). Biofilms are always attached to a substance, consisting of cohered microorganisms (10-25%) and are embedded in an extracellular polymeric substances matrix (75-90%). EPS is a complex composition, of various polymeric substances from polysacccarides, proteins, lipids, uronic acids etc. and parts and excretions of microorganisms. The embedding in EPS, provides the micororganisms in liquid media, the additional benefit is that they cannot be washed away into the soil.(Pal and Paul, 2008)

Relevance

Biofilms and EPS often cause problems by clogging wastewater systems (Kanematsu and Barry, 2020), risking food safety in the food industry (Galié et al., 2018) or in the pathogenesis by e.g. causing cardiovascular infections (Vestby et al., 2020). On the contrary, they can be used in plant protection, bioremediation or wastewater treatment (Muhammad et al., 2020). In the application of microfluidic devices biofilms have also both, negative and positive attributes. The formation of streamers can lead to problems such as clogging of biomedical devices like stents, catheters etc. or can lead to flow structure interactions (Drescher et al., 2013). On the other hand, biofilms can be used to create novel bio-mediated structured materials, like we have seen from Liu et al., 2017, where nanocellulose-glassfiber nanocomposites, with nanocellulose oriented with electromagnetic fiels was produces, or from Kondo and Kasai, 2014, who have successfully fabricated 3D honeycomb structures from bacterial cellulose. Also in the microfluidic cell under investigation, biofilm formation is the central element for material production. The EPS strands, which often lead to problems, are to be oriented by the porous structure of the microfluidic cell and mineralized in a later process.The CFD study of fluid flow and biofilm distribution, can increase the understanding of this phenomenon and lead to the improvement of EPS structuring.

Biofilm growth

The biofilms adhering inside the microfluidic cell interact, during their growth cycle, with the microfluidic cell material (polydimethylsiloxane) via chemical, physical and biological processes and are influenced in this way in their buildup process. The basic four steps in the formation of biofilms with microorganism like we used in the study (*K. xylinus*), described from Vasudevan, 2014, consist of initial contact with the surface (1), reversible adhesion (2), irreversible adhesion (3) and biofilm maturation and dispersal (4). In the first

phase, primary contact with the surface occurs via passive movement (gravitational forces or brownian motion). In step two, the reversible attachment of the bacteria to the surface takes place, passing through electrostatic and hydrodynamic interactions. The interactions can be strongly influenced by pH, temperature or ionic forces. The material of the surface plays an important role in the adhesion as well, as hydrophobicity is preferred. In a third step, the irreversible adhesion takes place, which happens by fimbria. In the last steps, the maturation of the biofilm and the biofilm detachment takes place, with a subsequent restart of the whole cycle. The bacterial movement process in fluids is closely related to the rheotactic behavior of various bacteria. Rheotaxis is the ability of a bacterium to react to environmental stimuli, more precisely to fluid flows. The microorganism can be induced to a swimming motion by the velocity gradients and the helical shape of flagella. This mechanism is essential for the dispersal and movement of microorganisms and is also the main mechanism for bacterial movement in our study. (Marcos et al., 2012)

Biostreamer

In hydrodynamic flows, so-called streamers have been reported. Streamers are generated by bacterial biofilms and have a filamentous morphology. They have been observed in porous media and are typically attached to a solid surface at one or both ends, while the rest is suspended in the liquid medium. (Hassanpourfard et al., 2015) Streamer formation has been observed in both high Reynolds number flows (Stoodley et al., 1998; P et al., 2002,) and low Reynolds number flows (Rusconi et al., 2011; Marty et al., 2012) and has been sufficiently studied. How streamer network formation relates to hydrodynamics has been little explored, but has influence in porous media, as both change in friction factor and pressure drop are suspected (Valiei et al., 2012). The artificially produced porous structure of the microfluidic cell is supposed to use exactly this streamer formation and to form structured EPS by directed guidance of the streamers. Therefore, both streamer formation and the influence of the streamers in the flow must be understood.

1.2.2 Issues to be solved

While the formation of biofilms is already well advanced in research, the formation of streamers and especially the formation of streamers in porous structures is still partly unexplored. It is not clear yet which hydrodynamic processes play the main role in the rheotactic behavior of biofilms and the formation of streamers in microfluidic cells. Studies have shown, that the secondary flow in curved structures, are responsible for the formation of biofilm streamers (Rusconi et al., 2010; Drescher et al., 2013). This could also be be the case for microfluidic cells. Another explanation is the theory, that biostreamer form as highly viscous liquid jets, directed by the flow (Das and Kumar, 2014). Understanding the formation of biostreamers in porous structures cannot only give a significant contribution in bio-mediated material synthesis but can also help avoid the negative impacts of biostreamers. Another open question is

the adhesion of the bacteria to the micropillar. Although the principles of the bacterial adhesion on surfaces are well studied, it is not yet known exactly how this adhesion occurs in relation to shear forces occuring in the microfluidic cell. Here, based on the studies, of Valiei et al., 2012 and Hassanpourfard et al., 2015 it has been observed that the attachment of the bacteria strongly depends on the force occurring on the micro pillar of the cell. In addition, it is assumed that a critical point exists that causes more biofilm to vanish than to adhere.

1.3 Microfluidic cells and the application in materials science

In order to better understand how microfluidic cells are used in material synthesis and why it is relevant to analyze the microfluidic cell present in the thesis, an introduction to the topic is given in the following sections.

1.3.1 Introduction to microfluidics

Microfluidics is a science and technology that describes fluid flows on a micro or nanometer scale. It deals with fluid behavior at these scales and the ability to fabricate micromechanical structures. (Aryasomayajula et al., 2017). A key element of microfluidics is to analyse this fluid behavior in appropriate scale, which is enabled by the production of microfluidic chips. One way of using microfluidics is the production of microfluidic chips. Microfluidic chips are miniaturized cells with a pattern of microchannels, typically in the size range of 5-500 μm and fluid flows from mikroliter to femtoliters .(Weibel and Whitesides, 2006)

The application of microfluidic devices is a relatively new technology, which is becoming more and more important today. The first similar devices were produced in 1980 by the first silicon etching and were used in the electronics industry. However, the technology only gained importance in the 2000s when it became possible to etch microchannels in polymers in order to save costs and time. (Saxena and Joshi, 2020). Nowadays, microfluidic cells can be made of different materials such as glass, plastic or silicone. Nevertheless, the most widespread and widely used manufacturing method today is lithography with polydimethylsiloxane as the starting material (Weibel and Whitesides, 2006), as it is also used in the microfluidic cell in the study. In this process, a mold is etched in silicone, which can then be cast. This method allows the fast creation of microfluidc devices that reduce experimental costs and accelerate the speed of research, which makes microfluidics more advantageous compared to other systems.

The main fields of application of microfluidic cells can be found in biomedical applications or cell biology reasearch, such as analytical arrays, gradients, separators, microdiluters, gel structures, droplets, painting cells and devices

(Weibel and Whitesides, 2006). There, the gradients are used, for example, to detect specific proteins in large samples (lab-on-a-chip).

Taxis and microfludics

The functioning of microfluidic cells is often tightly connected to the taxis of microorganism. The taxis is the ability of bacteria and organisms to respond to external stimuli. (Goldstein and Soyer, 2008). This thesis focuses mainly on rheotaxis, which will be elucidated in more detail in chapter 1.2. The rheotaxis, uses water or air currents as a means of orientation (Marcos et al., 2012), and responses in the case of our system, with the bacterial orientation in the direction of flow. The basic functional system of a microfluidic cell is that a fluid is firstly fed into an inlet to ensure good distribution, then into an area where a function is performed. In this thesis we focus on the bio-mediated material structuring of bacterial cellulose, which uses a chamber area with a micropillar structure, to guide a bacterial fluid through e wanted direction.

1.3.2 Microfluidics in materialscience

Microfluidics or the microfluidic cell are also used in materials science. In contrast to its use in biotechnology, however, the technology is still in the early stages of development. The microfludic system used in the thesis, builds on the principle of bio-mediated material structuring. bio-mediated material structuring is a way of transferring biological systems to materials. There is a classification system to divide the abstraction levels of this process into various levels. This classification ranges from level 0 abstraction, meaning the direct use of materials that have been chemically modified, to bioinspiration and biomorphism which represents level 4 .(Deuerling et al., 2018) In this thesis we focus on so- called bio-mediated material structuring (level 2), with three or more hierarchies involved. Basically, the target material in the study can be seen as a composite of organic and inorganic material, whereby the organic materials mostly have a hierarchical structure and the inorganic ones only partially.

Bio-mediated material structuring

Bio-mediated material structuring is characterized through the guidance of organism to create structures, that can be converted into materials or can already be used as an end product material. The methods by which the organisms can be guided can vary with the individual manufacturing processes. The used cell in the study uses in line structured micropillar for the guidance of the fluid. The integral part of every mechanism is the need for a mechanism that actively places the organisms. This mechanism can be created by external forces (mechanical placement) or can be controlled by external activation of internal forces of the organism. Another possibility is the independence from external factors. This type of placement is relevant for the use of microfluidic cells and also determines the placement of the cell used in the

analysis. The main mechanism for this is the guiding or placement of organisms through mechanical contact, which can be made of structural elements synthetic materials, elements secreted by the organism or by the organism itself. This type of structuring requires the presence of a template or a flow to function.(Deuerling et al., 2018) We thus see that the geometry of the guiding device is of great relevance in bio-mediated material structuring. Considering the geometry of the study, this means that the analysis of the fluid flow around the micropillar can provide significant results in terms of structure formation.

Latest development

In recent years, research has been conducted in various directions to produce bio-mediated materials. For example has Qi et al., 2019 shown how to biomimetically (stage 3) mineralize nano fibrillar cellulose with hydroxyapatite to produce a material that resembles that of hard tissues. From Cheng et al., 2019, we have seen a bio-mediated system of bioinspired production of bone inspired mineralization to produce a hard material such as bone from highly alligned cellulose. Another way in bio-mediated material synthesis was shown from Spiesz et al., 2019 by alternately crystallize calcium carbonate and produce γ-polyglutamate (PGA) in a layered structure. The result is a material that resembles nacre and has its properties. The material had the advantage that unlike existing attempts to produce nacre, no toxic chemicals are used and thus a cost-effective and eco-friendly material composite material can be produced.The example thus shows that bio-mediated materials not only demonstrate new ways of producing materials, but can also produce improved, more cost-effective and eco-friendly materials.

The fact that microfluidic cells of various designs are already being used today to produce materials in particle form, fibrous form or as a sheets, has been vividly demonstrated by Ma, Wang, and Liu, 2017. The study shows that the fabrication of materials with microfluidic cells, in recent years has become increasingly simple and allowed more complex geometries. In addition, the materials could be made more complex and composited with other materials. Nevertheless, it is also shown that the technology is still improvable and needs further research.

1.3.3 Considerations for the design of microfluidic cells

The microfluidic cell investigated in the analysis is intended to be used for the production of rheotactic hierarchically structured materials and to advance research in this field. The microfluidic cell is structured in such a way that the fluid is guided by micropillars to form biofilm in an ordered structure via contact-based guidance (see geometry 3.8). The microfludic cell is considered a central element in the production process. In particular, the optimal flow guidance is essential to ensure the highest possible cell adhesion with high and structured EPS deposition. In addition, the optimal flow guidance and the understanding of it is relevant to prevent random EPS formation and clogging. Because the design of such a microfluidic cell for the production

of materials, has not yet been optimized, the analysis through the computational fluid dynamics and previous investigations is expected to lead to an improved geometry. It is expected, especially in the inlet area and around the micropillar, that geometric improvements could lead to an improvement of the flow and the EPS formation in the microfluidic cell,since the inlet region and the micropillar region have a guiding role in the microfluidic distribution and the complexity ends to lead to more errors.

1.4 Computational Fluid Dynamics

Experimental investigation of fluid dynamic processes within the microfluidic cell has its limitations, therefore we will analyse the cell using computational fluid dynamics (CFD). The following sections provide an introduction to CFD simulation and to the areas of hydrodynamics relevant to the project.

1.4.1 Introduction in CFD

Computational Fluid dynamics or CFD is a powerfull method to solve fluid dynamic problems, using a computer and numerical algorithms. It can simulate problems of fluid flow, heat flow, particle motion or other simultaneous reactions such as chemical reactions. The application fields of CFD are very wide and can be applied in hydrodynamics, aerodynamics, metereology, biomedical engineering and many other fields. (Versteeg and Malalasekera, 2006) Most fluid dynamic problems cannot be solved analytically and must therefore be determined either numerically or experimentally. However, experimental determinations in engineering applications are sometimes not feasible due to high experimental costs, complex setups, safety hazards or time constraints. Therefore, the use of CFD simulations can be beneficial in such situations. The continuous improvement of CFD programs has led to more accurate solutions and its frequent use in the field.

1.4.2 Conservation principles and turbulence modeling

To calculate the system to be solved, conservation equations are created from the space in the microfluidic cell. The equation can be given in various forms, but the most commonly refereed to version in CFD is the integral form, since the finite volume method is used as a discretization method for CFD. There are five conservation equations from fluid mechanics for a control volume (J. and M., 2008):

- Mass conservation
- Momentum conservation in x direction
- Momentum conservation in y direction
- Momentum conservation in z direction
- Energy conservation

For the complete conservation equations, see appendix B. The combined equations of mass, momentum and energy, in fluid dynamics are called the Navier-Stokes equations. These equations describe the relationships of pressure, temperature, density and the fluid motion in flows. For the solution, apart from the 5 conservation equations, additional 12 equations are needed, comprised of 3 state equations and 9 Stokes relations. The Stokes relations couple the stresses τ with the velocities (Lecheler, 2014). In addition, depending on the dimension up to 5 boundary conditions have to be given to solve the equation. The Navier Stokes equations have been solved analytically for very simplified cases and have otherwise to be solved numerically.

Simplifications

One of the main problems in the study of flows is the calculation of turbulence, which requires a lot of computational resources. The solution via the direct Navier Stokes equation (DNS), takes into account all turbulence, but has a sensitive system, needs a lot of computation time and a very fine mesh. To reduce computation time CFD programs in a first step, simplify the Navier-Stokes equation (DNS) by performing a Reynolds averaged Navier-Stokes equation (RANS). The RANS averages the flow magnitudes of the conservation equation over a period of time and forms them using mean variables and fluctuation variables to model turbulent flow. (Alfonsi, 2009) This mathematical decomposition, results in a new term called the Reynolds stress tensor. The Reynolds stress tensor is calculated in CFD simulations, with the help of turbulence models which simplify the modelling of turbulent flow. How well turbulent flows in a system are modeled depends on which turbulence model is selected for the specific system.

The most important turbulence models are according to Lecheler, 2014 listed below. Which turbulence model is used for which case is essential and determines the accuracy of the solution.

- **Laminar model** Does not take Reynolds stresses into consideration, since there is only laminar flow (no turbulence).
- **k-ϵ-model** Two transport equations for kinetic energy k and turbulent dissipation ϵ. It is less accurate near the wall, because of dissipation by pressure gradients.
- **k-ω-model** Two transport equations for kinetic energy k and turbulent frequence ω.It is more accurate near the wall, less accurate in the middle of the Stream.
- **SST-model** Combination of k-ϵ and k-ω. It provides better results near the wall and in the center of the flow.
- **LES,DES** Large eddy simulation and detached eddy simulation. Solve the equation transiently without Reynolds averaging.

We have seen that CFD performs complex modeling to represent turbulence. How accurate the later system is depends on how optimally one of the many turbulence models is fitted to the system. The optimal system can be found by excluding systems that do not fit, or by selecting a system with simulation-specific preferences. Often the accuracy of turbulence and the behavior on walls are relevant for the process. How the system is finally selected remains a subjective decision making process. The laminar system selected in the study, was chosen after an investigation and exclusion of the turbulent flows in the cell.

1.4.3 Numerical solution method

Discretization method

Discretization is the creation of continuous variables in finite differences. The discretization in CFD is done by three different systems of mesh generation, where each method can be transformed into the other. Next the tree main methods are shown:

- Finite difference discretization FD
- Finite volume discretization FV
- Finite element method FE

The discretization methods differ in accuracy and flexibility. FE is the most accurate and FD the most flexible. FV is used in CFD because both flexibility and accuracy are desired (Lecheler, 2014). FV creates a number of non-overlapping control volumes and uses the intefral form of the conservation equation as a starting point.

Computational Fluid dynamics distinguishes between spatial and time discretization. The method relevant for the study is the second order upwind scheme, which uses two data points to approximate the spatial derivate. The basic difference of the second order upwind scheme to the first order upwind scheme, is that the first order uses just one data point to approximate, is therefore more stable and faster but less accurate then the second order. The usage of the second order upwind scheme is preferred, for high quality meshes.

Computing Meshes

The creation of meshes in the geometry is crucial to whether the simulation converges or not. The CFD meshing program has several mesh types that can be adapted to the geometry. The simplest mesh is the cartesian mesh. The mesh has rectangular cells and has very small termination errors. This means that the Cartesian mesh leads to high accuracy. However, it should be noted that flows on geometries are difficult to calculate, since the mesh can only adapt poorly to non-straight geometries.The Cartesian mesh shows clear advantages in flows without contact to a geometry or in flows far away from

geometries. In order to adapt to any geometry, CFD tools can create skewed meshes. The skewed meshes are classified as O, C or H meshes depending on the shape of the mesh. Skewed computational meshes have higher termination errors, but behave better than Cartesian meshes at boundary layers of geometries. To achieve the best possible results the different meshes can be combined. In free flows Cartesian and flows on walls of geometry skew meshes. Thus, the quality of the solution can be increased to the maximum. In addition to structured meshes, unstructured meshes can also be created, for example, in 3D geometries . Unstructured meshes have no regularity and can take tetrahedral, hexadric, prismatic or other arbitrary shapes.(Lecheler, 2014)

1.4.4 Dimensionless quantities

"Dimensional analysis offers a method for reducing complex physical problems to the simplest (that is, most economical) form prior to obtaining a quantitative answer" (Sonin, 2001). Dimensionless quantities are characterized by the fact that two systems with the same value frame, e.g. same speed, different radius, can be compared with each other. The quantities do not have any units. Often, at certain values of dimensionless quantities, physical processes are observed, which occur at the same value for systems with different conditions, but the same ratios. They enable to compare or to analyze systems and to characterize physical processes or states. In fluid dynamics and also in this thesis, the dimensionless quantities are used to analyze flows and to identify various phenomena that occur. An important example of such a dimensionless quantity is the Reynolds number, which is a ratio of internal forces to viscous forces, and which evaluates the flow characteristics of geometries. The Reynolds number can be used to detect the transition from laminar flow to turbulent flow, or the occurence of the Kármán vortex street. The Kármán vortex street occures under specific flow conditions, and on bluff bodies so that alternating vortices with a certain frequency are created behind the body (Cooper, 2001). Other numbers relevant to fluid dynamics are the Knudsen number, which describes the flow behavior in gas flows, the Mach number, which is relevant to the speed of sound or the Strouhal number which characterizes oscillating flows. We will refer through various such dimensionsless quanitites throughout the thesis.

1.4.5 CFD in the microfluidic cell

The difficulty of CFD analysis in the microfluidic cell lies in the inlet region and the micropillars. The geometry, although only moderately complicated has many locations where high numbers of cells are required to achieve convergence. Similar analyses of microfludic cells, have already been performed (Liu and Li, 2013; Zhuang et al., 2019; Wei et al., 2015) to assess the distribution of fluid in the geometry from the inlet region. For the simulation of the chamber area there have been various studies (Hassanpourfard et al., 2015; Ichikawa, Yamamoto, and Motosuke, 2018; Secchi et al., 2019) with comparable systems that can be applied in our case as well. The work in the field, is

mainly directed in geometry improvement by CFD and flux behavior at the micropillar. The thesis is able to show both geometric and flow functions by looking at the whole cell and therefore shows larger correlations than in the studies before.

1.5 Aim of the Thesis

The analysis of the flow in microfluidic cells has been not been well explored and can be used particularly in the understanding and improvement of hydrodynamic processes in microfluidic cells and specifically in the microfluidic cell used in the study. The aim of the CFD investigation, is the analysis of the prevailing geometry and the detection of geometric improvement possibilities. In addition, the simulations will be used for general understanding of the hydrodynamic processes and rheotaxis of microorganisms in the microfluidic cell. The results will be used to contribute to a larger project in which the goal is to develop macroscopic monolithic and anisotropic hierarchical materials.

Both 2D and 3D investigations were performed. We investigated the general flow behavior, the flow at ascending velocity as well as the concentration increase of EPS formation in the cell, to analyze and describe the geometry characteristics. In addition, the secondary flow formation, the formation of wall shear forces, and the formation of turbulent flows in the system were studied to describe the flow behavior. The analysis of the geometry is needed to improve the fluid flow in the microfluidic cell and to create a more uniform layer structure for the later usage in materials science.

Chapter 2

Methods

In the following chapters, the different methods used in the thesis are explained.

2.1 Biofilm growth experiments

The experiments for the bacterial growth were carried out before the start of the thesis but are relevant for the understanding of the further work. The resulting data were available for the analysis.

2.1.1 Fabrication of the microfluidic cell

The fabrication process described is based on Klotz et al., 2021. For each experiment for the extracellular polymeric substances growth experiment were new microfluidic cell cast. For the validation experiments (2.5.1) were three microfluidic cells cast.

For the production of the master mold for the later casting, silicone wafers were coated via photolythography to create the microfluidic cell pattern on the wafer. In a second step, the created pattern were transferred to the wafers via a substracting etching process to create a master mold. For the production of the PDMS microfludic cells, the silicon master mold was placed in a mold with prefabricated connections for the in and outlets, cast with PDMS (SYLGARD™ 184 Silicone Elastomer Kit, Mixture Silicone/Initiator 1/10, Dow Chemical, Midland, United States), freed from bubbles and polymerized for 24 h at 45 C°. The microfluidic cell was completed by removing the PDMS stamp from the master mold and applying a sealing glass to the open top by a 45 s plasma treatment.

2.1.2 Bacterial culture

The bacterial culture used for the experiments was *Komagataeibacter xylinus* strain DSM 2004, obtained from the Deutsche Sammlung von Mikroorganismen und Zellkulturen (DSMZ, Braunschweig, Germany). In a first step the *K.xylinus* bacterium on an agar plate was inoculated subjected to a growth phase in a batch culture of 150 ml DSMZ Medium, containing 100 g l^{-1} Glucose (VWR International, Darmstadt, Germany), 10 g l^{-1} yeast extract (VWR International, Darmstadt, Germany) and 20 g l^{-1} $CaCO_3$ (Carl Roth, Karlsruhe, Germany) at pH 6.8 . The culture, was subjected to a growth phase,

in ambient temperature, until it reached the stationary phase, to use it for the experiment. (Klotz et al., 2021)

2.1.3 Experimental Setup and execution of the experiment

Figure 2.1 shows the experimental setup, used for the biofilm growth experiments and for the validation (2.5.1).

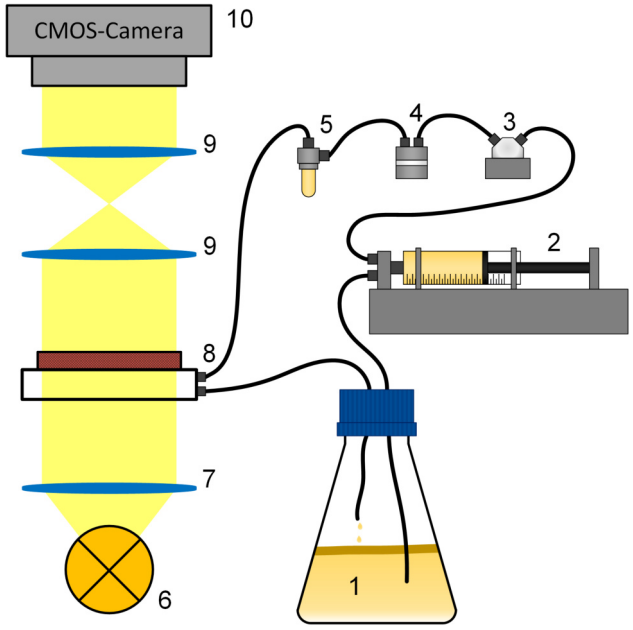

FIGURE 2.1: **Overview of experimental design.** Graphic from (Klotz et al., 2021). **(1)** Mature bacterial culture in an Erlenmeyer flask, tube towards pump inside the liquid, return so that tube is outside the liquid at atmospheric condition. **(2)** Syringe pump for the suction process and continuous pumping into the system. **(3)** Membrane pressure sensor with connection to syringe pump to avoid overpressure and ensure continuous flow **(4,5)** Bubble traps, prevention of air bubble transport into the cell. **(6)** Light source for the camera system. **(7,9)** Mirror system, Light settings and light redirections for the camera. **(8)** Microfluidic cell, mounted horizontally. Lighted for the camera and connected to the inlet and outlet of the bacterial solution. **(10)** CMOS-Camera sensor, For capturing black and white images of the microfluidic cell.

The stationary bacterial batch culture, was introduced into the microfluidic cell by syringe pump (neMESYS 290N with QmixElements, CETONI, Korbussen, Germany). The set syringe injection rates are shown in the table 2.1. Based on the average cell velocities to be achieved, the syringe injection rate was calculated. The fluid was first passed into the membrane pressure sensor (CPS 2184 Z, 5 bar, CETONI, Korbussen, Germany) connected to the syringe system, which was used to control the fluid flow and prevent overpressures of 1 bar in the system. In order to avoid bubbles in the microfluidic cell, the liquid was passed in a second step through two bubble traps. One for larger bubbles with a membrane system in the starting phase (Bubble Trap

for Microfluidics, ELVEFLOW,Paris, France) and the second bubble trap (Microfluidic Reservoir XS, ELVEFLOW, Paris, France) for smaller bubbles with a reservoir system. In a final step, the liquid was passed through the microfluidic cell and back into the flask (Klotz et al., 2021).

TABLE 2.1: Calculated mean flow rates and pump injection rates.

Flow rate/(mm s^{-1})	Syringe injection rate/(μl s^{-1})
1.0	0.450
12.5	5.625
25	11.25

During the execution, 8-bit black/white images were recorded every ten minutes. 29 experiments were carried out, of which 12 were considered for further analysis. The other experiments had to be discarded due to contamination by air bubbles and clogging by small particles.

2.2 Simulation

The simulations were performed according to the standard procedure described in (Lecheler, 2014) and was supplemented with (J. and M., 2008).

2.2.1 Performed simulations

2D as well as 3D simulations were performed. The 2D simulations were performed in a first step with five different mesh resolutions to perform the grid independence study (3.2). In a second step, the 2D simulations were performed with the three defined velocities. These were carried out with laminar turbulence model as well as with turbulent turbulence model (k-Ω-SST). The turbulent model was excluded afterwards (3.5). In a third step, transient simulations with all three velocities were performed for the 2D model. For the determination of the turbulent flows in the system, simulations with higher velocities as critical Reynolds were performed, but not considered further due to irrelevance (3.5). As a suggestion for improvement, new simulations with corrected geometry was performed.
Also for the 3D simulation with the shortened inlet (2.2.3), five simulations with five different mesh resolutions were performed for the grid independence study. Furthermore, a simulation with the entire geometry was performed. The simulation was used to determine the reference pressure difference for the validation (2.5.1). For the secondary flow tests, three simulations were performed with each of the three defined velocities. In order to determine the approximate pressure in the pipes, simulations were carried out with a special geometry that was intended to imitate the real pipe length. The simulation served only as an overview but was not used for validation.

2.2.2 Conditions, assumptions and simplifications

The working fluid defined was a mixture of water and bacterial culture with a dynamic viscosity of μ = 0.00134 Pa·s and a density ρ = 995.8 kg m^{-3} and was considered as homogeneous. The conditions of the bacterial solution, were determined in a previous experiment. The density of the wall material (Polydimethylsiloxane) was set as 965 kg m^{-3}. For the simulation the average chamber velocities were converted to inlet velocities. The final inlet velocities used for the simulation were 9 mm s^{-3}, 130 mm s^{-3} and 225 mm s^{-3}. As the flow rates and Reynolds numbers were low, the flow was considered as incompressible, laminar and steady state. Additionally the system was set as isothermal and without any gravity effects.

2.2.3 Geometries

The geometries were created with ANSYS SpaceClaim (Ansys, Pennsylvania, USA) and correspond to the masses of the original geometry used in the experiments. Figure 2.2 shows both the 2D geometry and the 3D geometry. In addition, the figure shows the different measuring points for the analysis.

2D-Geometry

The 2D geometry consists of the basic parts inlet area, chamber area and outlet area. The inlet area can in turn be divided into two inlets. Inlet 1 for the input of the microbial liquid and Inlet 2 for the input of alcohol as flushing agent. Only Inlet 1 was relevant for the simulation and will therefore be referred to as Inlet in the further course of this paper. The inlet area starts with one channel ($\varnothing 1\,mm$) and branches in a bifucurational of four stages into 16 channels ($\varnothing$ 0.5 mm) leading into the chamber area. It it not considered that the liquid does not flow into the cell as shown, but in an arc perpendicular to the considered surface. The chamber area consists of rows of 22x19 (418) arranged micropillars with a diameter of 50 μm and a distance from pillar to pillar of 0.5 mm. The outlet area is conical shaped and has an outlet chanel with a diameter of 1 mm. The whole cell has a width of 9 mm. The cell has no z-direction in the 2D domain and was calculated according to the default settings of ANSYS. The assumption, for the 2D simulation was made, because the flow was seen as fully formed (Thomen et al., 2017).

3D-Geometry

To simplify the 3D geometry, the inlet was cut off. This simplification were made because the 3D simulation was only needed in the chamber (3.7.2) and therefore the inlet plays a minor role. The simplification allows the increase of the cells in the chamber, which simplifies the achievement of a convergent solution. In addition, the inlet velocities can be adjusted as desired, since there are now several inlets. The depth of the cell was set to 50 μm, like the real cell.

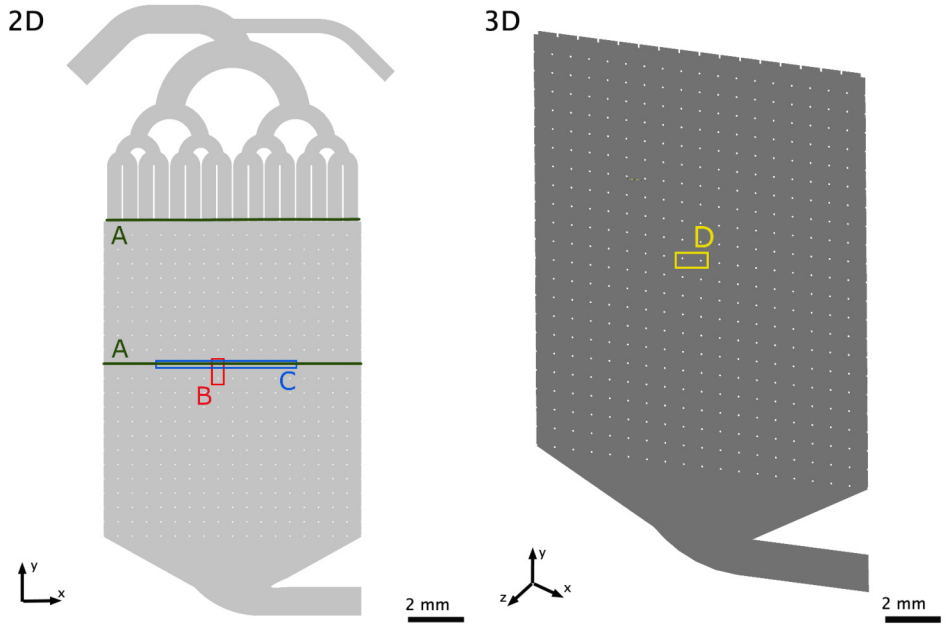

FIGURE 2.2: **Geometries and the measurement locations. (2D)** Geometry used for the 2D simulations with all measuring points in xy-view. *(A)* Measuring point for the velocity measurement at the entrance of the chamber area and in the middle of the chamber area for figure (3.4). *(B)* Section of the simulation of the wall shear forces on the micropillar for figure (3.7). *(C)* Section used for the determination of wall shear forces on the walls of the micropillars (3.8). (**3D**) Geometry used for the 3D-simulations in xyz-view with the measuring section. The cut-off inlet section visible. *(D)* Used section for the qualitative analysis of the flow and secondary flows in the chamber for figure (3.7)

.

2.2.4 Meshing

The mesh for the geometries was created with the ANSYS Meshing Tool (Ansys, Pennsylvania, USA) using the finite volume method. The system was equipped with a standard mesh and then continuously refined. The refinement was done by global refinement of the mesh through subjectively decided reduction of cell sizes and locally by gradiual refinement of the mesh at complex locations such as micropillar and inlet section. A quadratic structure of the mesh for the 2D object was selected. The 3D grid was meshed with a hexahedral structure. Since the element sizes in the system were smaller than the calculated maximum wall boundary layer and the flow was considered laminar, the wall boundary layer was not considered as relevant. To create the optimal mesh a grid independence study was conducted.

2.2.5 Grid quality

The quality of the created meshes was assessed and adjusted by the typical CFD quality characteristics listed below. The values achieved are shown in the result section in table 3.2.

Skewness

The skewness defined for all cell shapes (2D and 3D) was defined as follows:

$$S = max\left(\frac{\alpha - \alpha_{opt}}{180^{\circ} - \alpha_{opt}}, \frac{\alpha_{opt} - \alpha}{\alpha_{opt}}\right) \tag{2.1}$$

Where:

S = skewness

α = largest angle in the cell

α_{opt} = optimal angle

The skewness S calculated with the formula 2.1 shows how similar the ideal geometric body is to the generated body is. In the ideal case the skewness can reach S = 0 and in the degenerate case S=1. Recommended for CFD simulations is a mean value of minimum S = 0.1 for 2D and S = 0.4 for 3D simulations. The grid should not contain cells with skewness above 0.95.

Aspect ratio and orthogonality

The aspect ratio is defined as the ratio between the longest and the shortest edge length of a created mesh cell. The best possible aspect ratio is A=1 the other ratios are always higher. A good quality mesh showes aspect rations below A < 35. To high aspect ratios, cause systems not to converge.

The orthogonality is a quality value calculated via vector mechanics. The value can take reach from O = 0.001 (sliver) to O = 1 (optimum). The average orthogonal value of the system should be at least 0,2.

2.2.6 Simulation and Solver setup

The analysis of the microfludic cell was performed with ANSYS FLUENT (Ansys,Pennsylvania, USA). laminar turbulence model was selected for the calculation, as the Reynolds calculation indicates laminar flow. The boundary conditions at the walls were considered as non slip and the pressure at the outlet as atmospheric. For the pressure-velocity coupling the coupled method was used. For discretization, «second order upwind» method was chosen for pressure and «second order upwind» for momentum. The convergence criterias were set at 10^{-10} for all equations. In addition to the residuals, own report definitions were created. For the report definitions, the force acting on two different micropillars in the chamber and the drag force on a separator in

the inlet were defined, plotted, monitored and specified with a convergence condition criterion of 10^{-6}. The calculation was initialised via the hybrid initialisation. The inlet velocities chosen for the fluid were 9 mm s^{-1}, 130 mm s^{-1} and 225 mm s^{-1}.

2.2.7 Visualisation of simulation

The solutions were visualised with Ansys CFD-Post (Ansys,Pennsylvania, USA). In addition to the CFD-Post visualisations, graphics were created using Python. The data was taken from CFD-Post and exported to Python. The plots were all plotted at steady state flow in the cell.

2.3 Grid independence study

A grid independence study was performed for both the 2D and the 3D System using, five different resoluted meshes in quadratic structure (2D) respectively hexahedral strucure (3D). The mesh refinements defined can be seen in table 2.2. Five simulations were performed with each of the defined meshes. The simulations were carried out with an inlet velocity of 1 mm s^{-1} and with laminar and k-ω-SST model. The rest of the settings were left at the default settings. That means five simulations with different mesh finenesses were performed with two different systems, resulting in ten simulations. For the simulations, forces or drag forces were defined as measurement variables, which were read out for each simulation. The measuring points were located at four separators (stage 3) of the inlet on the one hand and at two micropillars at the top left and bottom right of the chamber area on the other hand. The resulting velocities were read out and compared both in a diagram and numerically. The grid independence study can be seen in the results section in table 3.2.

In order to integrate a differentiated mesh into the grid independence study, triangular meshes were created in addition to the square structured meshes. However, since these did not converge, they were left outside the system.

TABLE 2.2: Mesh refinements defined for the calculation for both 2D and 3D objects

	Very-coarse	Coarse	Medium	Fine	Extra-fine
2D-Object	118347	169108	190370	234714	271818
3D-Object	207324	334912	426375	474120	491925

2.4 Conversion and exclusion calculation

In order to complete the initial or boundary conditions of the calculations or to exclude special cases, the calculations or simulations described below were performed.

To convert the volumetric flow rate of the syringe pump, used in the experiment (2.1), to the velocity of the inlet of the simulation, the volumetric flow rates of the experiment were converted to the velocity via the area of the inlet. The volume flows of the syringe pump, are all already converted for the experiment from the desired average chamber velocity through the geometry of the cell.

To select the turbulence model of the simulation, the results of the Reynolds calculation (3.5) were used to exclude turbulent flows in the system and therefore a laminar turbulence model was chosen.

To exclude the formation of Kármán vortex effects, transient calculations were performed in addition to the Reynolds calculation (3.5). The transient calculations were performed with all three defined velocities of the simulation. The simulation was performed and visualized with 1000 time steps of a time step size of 0.2 s and 25 iterations per time step. In addition, report definitions of the force and the drag force were defined on two randomly selected micropillars. This enabled the visualization of possible oscillations of the values as Kármán vortex effects. Since the transient simulation did not show any oscillation behind the pillars, the effect was ignored.

2.5 Validation

Two measurable values were considered to validate the simulation. The pressure difference in the cell, since the pressure was the only physically measurable value for validation and the concentration analysis in the cell to confirm the predictions of the simulation and to complement the pressure difference if not suitable.

2.5.1 Pressure validation experiment

A pressure measurement was selected for the validation experiments. The reason was because the pressure in the system was the only parameter that can be measured both in the simulation and in the experiment with the existing measuring equipment. The measurements were all made with the pressure gauge of the syringe system. The basic setup of the experiments was set up in the same way as the experimental setup in 2.1. Measurements were taken at each possible pressure measurement point at the interfaces between the equipment and the pipes, to measure every path in the system. The fluid used for the measurement was water. In the first step, the microfluidic cells used for the bacteria growth experiments were inserted and measured and

recorded at each interface in five cycles each. In the second step, the micropillar structure of the microfluidic cell was manually scraped out to create a hollow microfluidic cell. This was measured exactly the same as in step one and recorded in five cycles for each measurement point. The resulting pressure difference, gives us the approximate pressure in the microfluidic cell. To measure the offset of the instrument, the output pressure of the instrument was measured without the instrument being connected.

2.5.2 Image analysis

In order to establish a reference to the real bacterial growth experiments with the simulation, the images generated during the experiment was analysed in an image analysis. The microfluidic cell was divided into four areas for the analyis (2.3). The precipitated cellulose was detected in the images as a change in the grey scale. The images taken in one hour intervals were compared in sequence with the first image free of cellulose. This change in grey level was described with the concentration c of the cellulose (g cm^{-3}). The concentration was determined via the Beer-Lambert law. The Beer-Lambert law describes: "a relation concerning the absorption of radiant energy by an absorbing medium.[...]The relationship can be expressed as A=ϵlc where A is absorbance, ϵ is the molar extinction coefficient (which depends on the nature of the chemical and the wavelength of the light used), l is the length of the path light must travel in the solution in centimetres, and c is the concentration of a given solution." *Beer's law | Definition, Equation, Facts | Britannica* Absorbance A and coeficient ϵ were determined in previous experiments by Klotz et al., 2021. The length l is the thickness of the microfluidic cell (50 μm). The cell could thus be analyzed, each in the four divided image areas, by the concentration change. Thus the correlation between the flow and the cellulose deposition in the individual areas is analyzed.

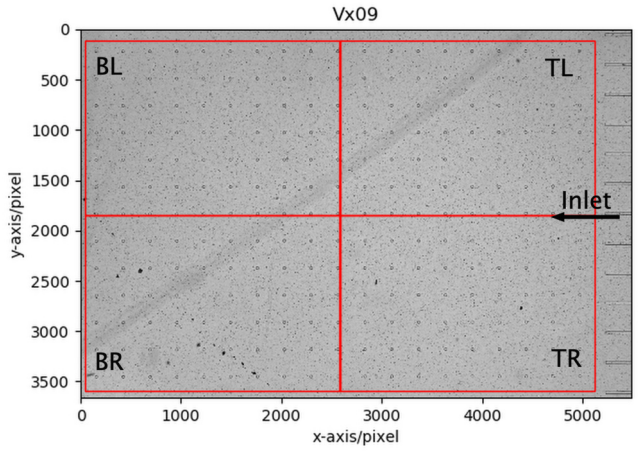

d

FIGURE 2.3: **Example cell of experiment** divided into the four areas. Flow from right to left. Divided in such a way that it can be compared with the simulated geometry (set up). Therefore divided into **BL** Bottom left, **BR** Bottom Right, **TL** Top Left and **TR** Top Right.The rectangular zones have a size of 2545x1745 pixels. The borders are always 130 pixels from the center of the micropillar.

Chapter 3

Results

3.1 Biofilm and EPS growth in the microfluidic cell

In a first step, we want to understand how the biofilm and EPS formation takes place in the microfluidic cell and what influence the speed has on the growth. The data for the following subsections, are based on experiments already carried out before the study.

3.1.1 Increase in velocity leads to a limit of EPS generation

To understand, how the biofilm and EPS growth behaves by increasing the fluid flow throughout the cell, we analyzed the concentration build-up as velocity was increased. We consider the analysis of the increase in concentration in the whole cell. The analysis shows us how the raise in velocity is related to the deposition of cellulose in the whole cell and gives us first understanding of the real EPS deposition process.

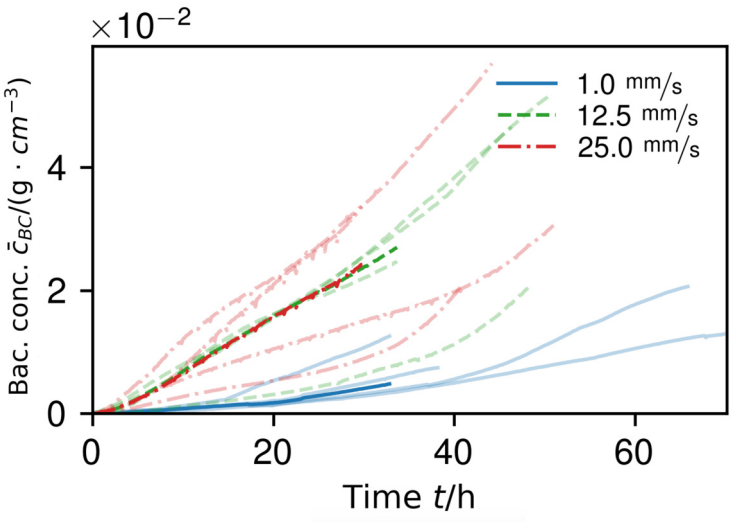

FIGURE 3.1: **Bacterial growth in whole microfluidc cell with increasing velocities** Graph from (Klotz et al., 2021). The increase in concentration of cellulose with time is shown. All experiments are plotted and color-coded according to velocity. The light color plots show individual experiments, the darker color plots the median values with standard deviation.

The concentrations in the cells in figure 3.1 show that increasing the velocity from 1 mm s^{-1} to 12.5 mm s^{-1} results in an increase in the concentration of Biofilm and EPS in the microfluidic cell proportional to the rise in velocity. The increase in velocity from 12.5 mm s^{-1} to 25 mm s^{-1} shows no further significant rise in concentration in the system. While at 1 mm s^{-1} we can see that the concentration increases steadily at about the same rate, at 12.5 mm s^{-1} and 25 mm s^{-1} it is no longer apparent how the increase in velocity is related to the increase in concentration. The mean values for the two higher velocities have shown that they are on the same line.

3.1.2 Influence of velocity on the structuring of biofilm formation

To understand how EPS formation occurs in the cell, we observed next the how EPS formation occurs in the cell, by qualitatively analyzing images of EPS formation.

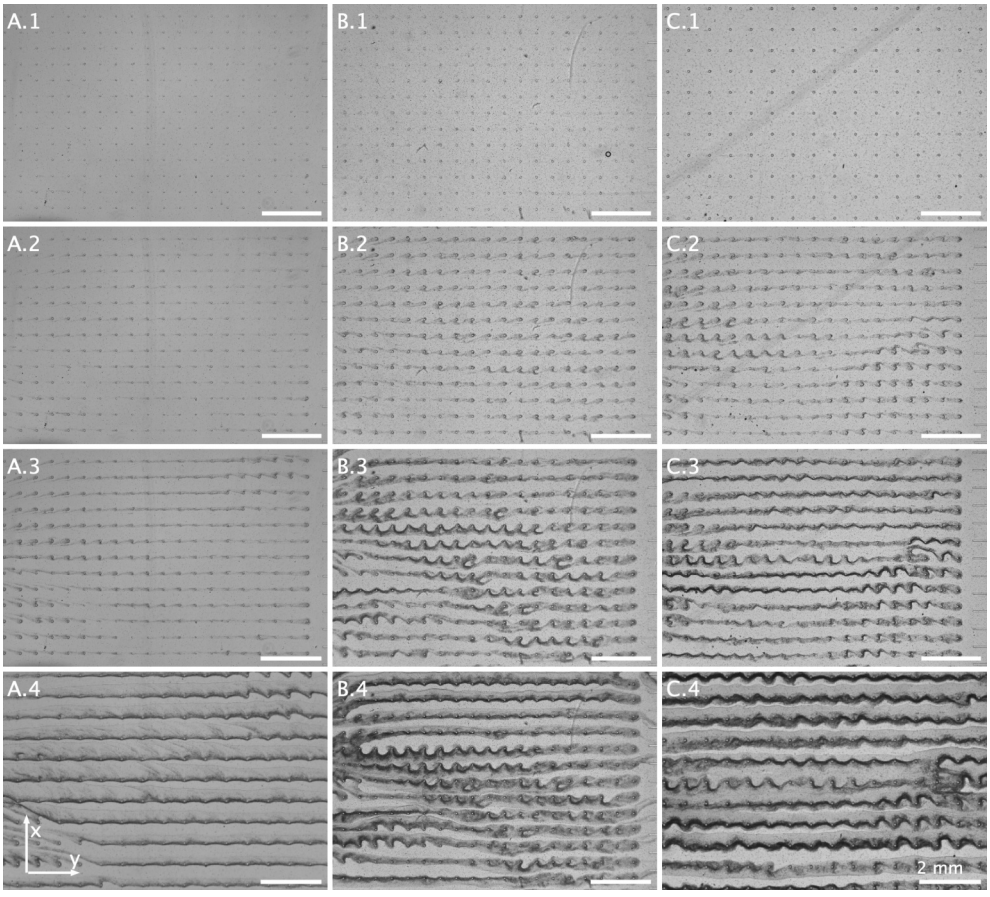

FIGURE 3.2: **Biofilm and EPS deposition in random chosen experiments.** Representation as in figure 2.3. Fluid flow from right to left. The gray streaks show biofilm and the extracellular polymeric substances. **(A)** Shows experiment Number Vx1 with the chamber velocity of 1 mm s^{-1}. **(B)** Shows experiment Number Vx26 with the chamber velocity of 12.5 mm s^{-1}. **(C)** Shows experiment Number Vx18 with the chamber velocity of 25 mm s^{-1}. **(X.1)** Image of the cell after 100 minutes. **(X.2)** Image of the cell after 6 h. **(X.3)** Image of the cell after 12 h. **(X.4)** Image of the cell after 24 h.

In a first step, we consider phenomena that occur at all three velocities. In the images (3.2 **X.1**) we can observe forall images at time 100 minutes, that the microfluidic cells seem still free of Biofilm and EPS. If we compare images **X.2** with images **X.1**, we can already see after 6h that biofilm on the left side of the micropillar appears in a small spikes. These spikes are the first biostreamer formed. In various locations, slight connections between the micropillars can already be seen. On the left side (towards the outlet), it can be observed that the Biofilm no longer forms horizontally but is directed slightly obliquely from the outside to the inside. After 12h in image **X.3**, the connections between the micropillars are already clearly visible due to the dark streaks. Clear layer structures can be recognized in the direction of flow. The biostreamer have now completely assembled. The connections are often wave-shaped and vary in the thickness of the wave. While we can see rather straight connections on the outer sides, we observe stronger fluctuations in the center at the entrance and in the center at the exit. First transverse biofilms are visible in places in the middle of the entrance and outlet. If we look at the image after 24h at **X.4**, we see similar structures as in **X.3**, but more pronounced. The previous connections have strengthened and are more visible due to darker areas. The flow between the Biofilm and EPS strands is still present, but shows increasingly more transverse biofilms blocking the microfluidic cell and thus filling the layered structure. If all experiments of all medium chamber velocities are compared with each other, we can see that the speed of biofilm formation seems to differ fundamentally between the velocities. While after 12h in **B.3** and **C.3** fully formed biostreamers are already visible, in **A.3** they are still very weak. We can see this behavior at each time step between the images, although the quantitative increase in concentration between **B** and **C** is only slight. Qualitatively, we can see that the biofilms in **A** appear straighter and more ordered. The lines in **B** and **C** are often highly bent and appear more chaotic. In addition, in the experiments with higher velocities, strong transverse biostreamer formations are evident in the middle of the cell.

3.2 Generated mesh quality and grid independence study

Before the simulation could be performed, a grid independence study was carried out and the quality of the mesh was checked. The grid independence study simplifies the simulation in so far as the number of grids can be reduced and thus computing time can be saved. The Grid independence study is a testing process to find the optimal grid (smallest grid number) that does not generate a difference in the numerical results. When a solution is sufficiently exact is defined on the subjective judgement (Lee et al., 2020). The quality of the mesh determines whether a convergent solution can be achieved and whether the solution meets the requirements.

3.2.1 Grid independence study

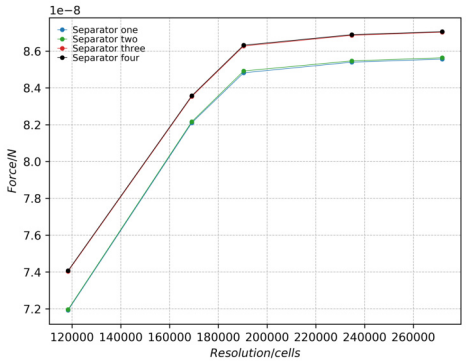

FIGURE 3.3: **Graphical grid independence study** Depicted are the four forces occurring on the separators (stage 3) with increasing cell resolution.Left part of the cell (blue and green) and right part (red and black).

The grid independence study was performed numerically and represented graphically to show the convergence of the quantities at the separators as an example. Table 3.1 shows the results of the analysis relative to the finest mesh in percent. The graphical analysis is shown in figure 3.3. The graphical solution shows the convergence of the forces occurring on the separators (stage 3) of the microfluidic cell, with increasing number of cells. Graphically we can see qualitatively that from mesh fineness size 4 to mesh size 5 no further significant differences are visible.

TABLE 3.1: **Grid independence study.** Both 2D and 3D objects divided into 5 mesh refinements. The calculated results for each mesh level are set relative to the result of the finest mesh. The result shows the mean value of all six measuring points.

2D-Object	Very-coarse	Coarse	Medium	Fine	Extra-fine
Number of cells [n]	118347	169108	190370	234714	271818
Relative [%]	12.4	2.79	0.743	0.157	0
3D-Object					
Number of cells [n]	207324	334912	426375	474120	491925
Relative [%]	21.6	4.67	1.61	0.106	0

In a quantitative perspective, we can see in table 3.1 that between the last two meshes for the 2D analysis there is a relative difference of 0.157%, respectively for the 3D analysis there is a relative difference of 0.106% of the results, between the fine and the extra fine grid. Both analyses show that with

an increasing cell density, the solution converges to a certain point and it is therefore evident that from the fine mesh onwards there are no longer significant changes of the result. Since the values seem to converge from the fine mesh onwards and the difference to the finest mesh is less than 1%, for the 2D analysis in the further, the simulations were performed with a mesh size of 234'714 and for the 3D analysis 474'120, to optimize time and computer performance. Whether the value is sufficient was decided subjectively and with the inclusion of experience values.
In addition, the difference in mass flow between the outlet and inlet was calculated with increasing mesh size to include another possibility for confirmation. The difference in mass flow for the selected mesh was $-5.45e-12$ kg/s. Considering the mass flow of $4.5e-7$ kg/s in the system, this means that a percentage mass of 0.001 % is dissipated per second. The mass losses do not lead to any relevant falsification of the results and can therefore be neglected.

3.2.2 Mesh quality

After the analysis of the grid independence study, the 2D mesh was created with a mesh fineness of 234'714 cells and for the 3D mesh 474'120 cells, respectively. The achieved quality of the mesh is shown in the table below. What the values mean and where the optimum level lies is described in chapter 2.2.4.

TABLE 3.2: **Mesh quality performance indicators.** For both, 2D and 3D, the typical CFD quality indicators are shown. As a reference the optimal values are displayed.

2D-Object	Reached values	Optimal value
Average skewness	0.183 ± 0.117	0
Orthogonal quality	0.964 ± 0.042	0
Aspect ratio	1.153 ± 0.138	A < 35
3D-Object		
Average skewness	0.223 ± 0.110	0
Orthogonal quality	0.951 ± 0.056	1
Aspect ratio	3.66 ± 2.048	A < 35

3.2.3 Pressure validation

In order to validate the simulation, a pressure based method was used to measure the pressure difference between the outlet and inlet of the microfluidic cell. In the table below, the results of the validation are shown.

TABLE 3.3: **Pressure validation** pressure difference between outlet and inlet

Δp Simulation [bar]	Δp Validation Experiment [bar]	Difference
0.1869	0.089	0.0979

We can see in table 3.3 that we have simulated a value twice as high as measured. The implications are described in chapter 4.4.

3.3 General flow behavior in the microfluidic cell

As a first step to understand the general flow behavior in the microfluidic cell, a contour plot was analyzed at mean cell velocities of 1 mm s^{-1}. The analysis of the general flow gives us indications of possible geometrical misconstructions and shows in a simple way how the fluid behaves in the microfluidic cell.

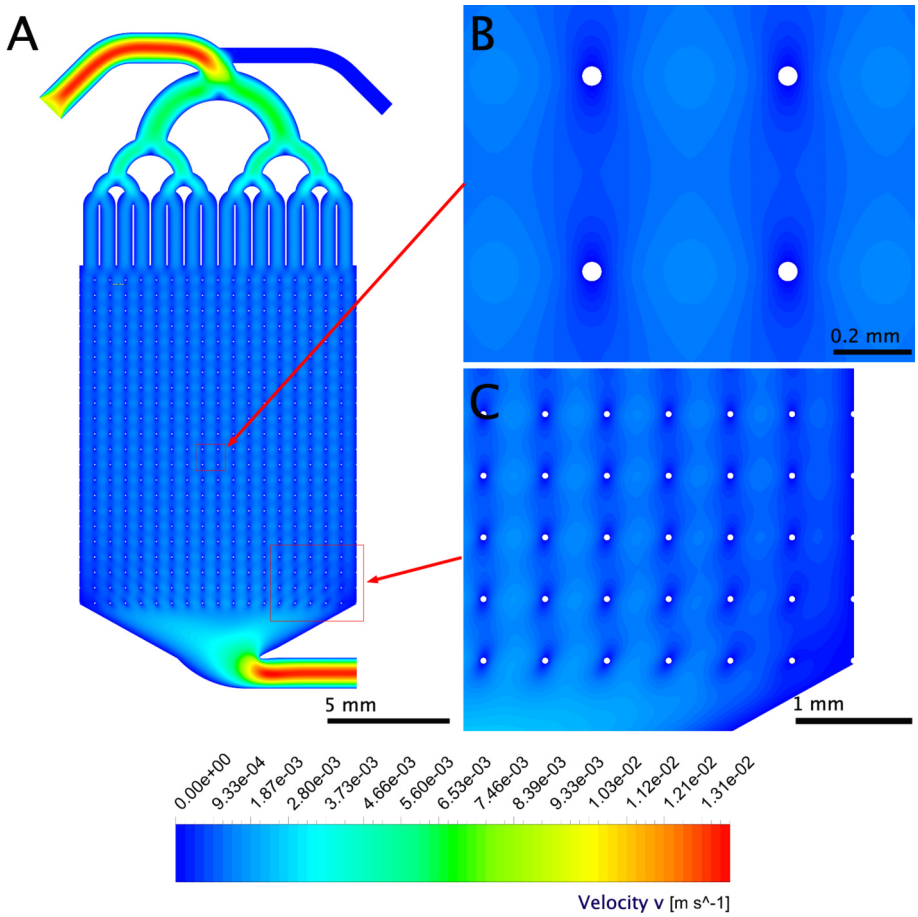

FIGURE 3.4: **Velocity contour plot with 1 mm s^{-1} mean cell velocity.** Linear color scale with range of velocities referred to whole cell **(A)** Entire microfluidic cell with inlet area, chamber area and outlet area. **(B)** Section of four micropillars in the center of the microfluidic cell **(C)** Section from the lower right side of the microfludic cell wall.

We can observe in figure 3.4 how the velocity of the fluid behaves in the microfluidic cell. We can clearly see that the fluid reaches the highest velocity in the inlet area and in the outlet area, with an approximate velocity of 130 mm s^{-1}. In the inlet area, we can see that the velocity in the first channel is slowed down at the sides and then decreases as the number of channels increases. In the chamber area, we see a qualitatively uniform distribution of velocity and fluid respectively. We observe that the fluid is slowed down at the micropillars. Above and below the micropillars, the fluid forms an oval

area, where the velocities are in a low range at 0-1 mm s^{-1}. The highest velocities in the chamber are found horizontally in the middle between the micropillars. In figure 3.4.**B** the maximum velocity is approximately 1.9 mm s^{-1}. Towards the outlet area, we can see that the velocities are not longer uniform. Especially when we look at 3.4 **C** it is observable, that fluid flow gaps occur the corners of the lower microfluidic cell.

3.4 Fluid distribution shift by velocity increase

In a next step, we analyzed the fluid flow in the cell as the velocity increased, such that we could observe the change in fluid flow that occurred in the process. The analysis shows whether the geometry is optimally designed, so that we see whether there is still a uniform distribution of the liquid if we increase the velocity. The optimal distribution of the bacterial fluid and the related biofilm growth is essential for the later use of the microfluidic cell, as only an optimally distributed biofilm respectively extracellular polymeric substance structure can give optimal results in the subsequent processing of mineralisation.

Contourplot

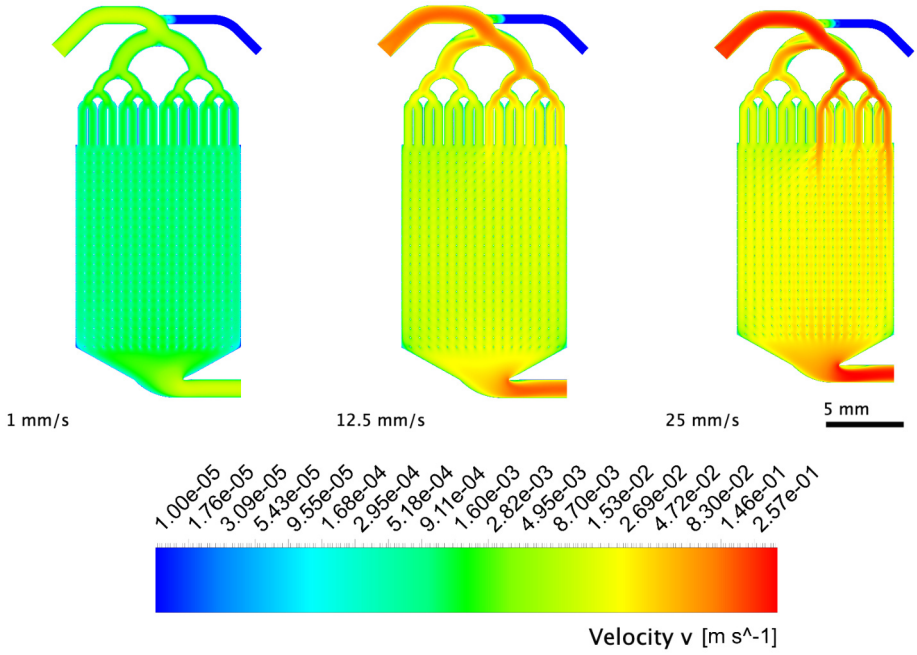

FIGURE 3.5: **Increasing velocities in the microfluidic cell** Entire microfluidic cell for all in the experiment used velocities. The compared cells are in a steady state and have the same settings and conditions. Logarithmic color scale used. **1 mm s^{-1}** on the left, **12.5 mm s^{-1}** in the middle and **25 mm s^{-1}** on the right

The figure 3.5 shows how the fluid distribution behaves with an increase in the flow velocities used in the experiment. It is particularly well recognizable

that with the increase of the velocity, the fluid distribution is shifted to the right part of the chamber. While at $1\,\mathrm{mm\,s^{-1}}$ average chamber velocity, no shift of the fluid fraction is evident, at $25\,\mathrm{mm\,s^{-1}}$ it is clearly seen that the fluid is pushed into manifolds 9, 13 and 16. At $12.5\,\mathrm{mm\,s^{-1}}$ the same distribution is evident with a lesser expression. As we have seen in 3.4 and now see on the left, in the upper half of the chamber, the fluid is uniformly distributed in the spaces between the micro pillars. In the lower half, the flow decreases on the outer sides and concentrates in the central part of the chamber. At $12.5\,\mathrm{mm\,s^{-1}}$ and $25\,\mathrm{mm\,s^{-1}}$ flow velocity, it is evident that despite the general redistribution of flow to the right side of the chamber, fluid movement occurs in all interstices except the outer sides of the lower part.

Chamber velocity

To get a different perspective on the velocity in the system, in a next step, the velocity at the entrance of the chamber and in the middle of the chamber were plotted. In this way it can be determined whether if there is a shift in the fluid distribution over the whole cell.

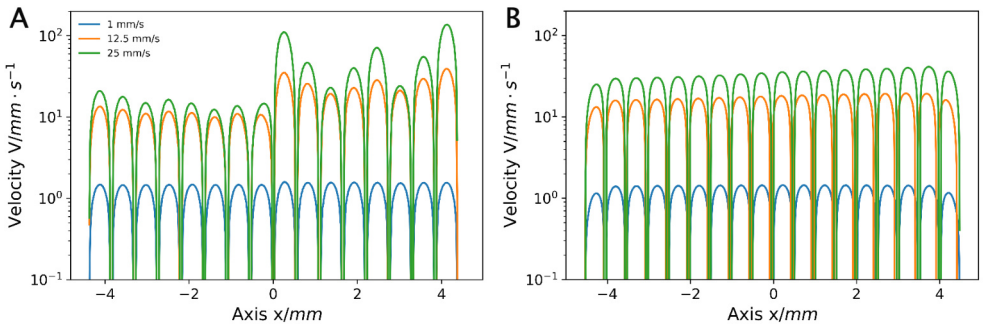

FIGURE 3.6: **Velocities in the microfluidic cell** The measurement locations can be seen in 2.2. The x-axis is set so that the zero point is in the center of the cell. The y-axis shows a logarithmic scale of velocity. *Blue* shows the 1 mm s^{-1} system, *orange* the 12.5 mm s^{-1} system and *green* the 25 mm s^{-1} system. **(A)** The velocities at the entrance of the chamber area. **(B)** The velocities in the middle of the chamber.

It can be seen that the velocity distribution for the system with $1\,\mathrm{mm\,s^{-1}}$ average chamber velocity exits almost uniformly from both, the inlet and in the middle of the chamber. An exception is seen in the middle of the chamber (figure 3.6.**B**), where the velocity on the outer sides is lower than in the rest of the measuring points. As already seen in chapter 3.5, at higher velocities, the peaks in outlets 9, 12 and 18 increase significantly. In the middle of the chamber (figure 3.6.**B**), on the other hand, we see that the peaks no longer have the same expression. The flow has a significant velocity redistribution in the right side of the chamber, but is more uniform than at the exit of the inlet region.

It can be seen that the average velocities of the higher velocity systems as they move into the center of the cell, change such that the relative deviation decreases, resulting in a more uniform flow than at the chamber inlet. At

TABLE 3.4: **Average maximum velocities in the chamber**. For both measurement locations, average velocities with relative standard deviation. The mean values, calculated from the peak velocities of the individual velocity cones. Standard deviation shown for all peak velocities of the velocity cones.

Velocity	Chamber entrance	Chamber center
1 mm s^{-1}	1.52 mm s^{-1} ± 3.3 %	1.4 mm s^{-1} ± 6.74 %
12.5 mm s^{-1}	19.9 mm s^{-1} ± 49.5 %	17.9 mm s^{-1} ± 6.74 %
25 mm s^{-1}	39.7mm s^{-1} ± 94 %	34.6 mm s^{-1} ± 13.3 %

1 mm s^{-1}, an increase in spread is evident as the fluid progresses to the center of the cell.

3.5 Exclusion of turbulent flows

Next, the possibility of the occurrence of turbulent flows at increased velocity was investigated. The analysis provides information about the flow behavior in the cell and is essential for the assessment of the flow behavior. The determination was done by calculating the Reynolds numbers (3.1) at the different geometries. In addition, the determination of the Reynolds numbers ensured that no Kármán vortex street occurs. The results of the calculations are shown below.

$$Re = \frac{v \cdot d}{\nu} \qquad \begin{aligned} Re &\ldots \text{Reynolds number } [-] \\ v &\ldots \text{velocity of the fluid } [\text{mm s}^{-1}] \\ d &\ldots \text{characteristic linear dimension } [\text{mm}] \\ \nu &\ldots \text{kinematic viscosity } [\text{mm}^2\,\text{s}^{-1}] \end{aligned} \tag{3.1}$$

TABLE 3.5: **Calculated Reynolds numbers**. Reynolds numbers calculated with highest velocity on each position. Dynamic viscosity of bacterial fluid ($\mu = 0.00134295$ Pa·s). For the calculation in different areas the characteristic linear dimension d was: inlet section (d = 1mm), micropillar (d = 50μm), sidewall chamber (d = 450 μm), sidewall outlet (d = 3.6 mm).

Position	**Re**$_{calc}$	**Re**$_{crit}$	
Inlet section	24	2100	(Menon, 2015)
Micropillar	3.7	40-90(Re_{kara}), 300-30'000 (Re_{krit})	(Sunden, 2008)
Sidewall chamber	20	150000-1500000	(Sforza, 2014)
Sidewall outlet	54	150000-1500000	(Sforza, 2014)

The results show that with the simulated velocities there is no theoretical possibility of turbulent flow in any of the existing geometries. In the inlet it is shown that at most a velocity of 0.33 m s^{-1} respectively a Reynolds number of 24 is present. The theoretical transition from laminar to turbulent in the geometry of the inlet is approximately 2100 (Menon, 2015). This means that for

the turbulent transition, inlet velocities of 32.6 m s^{-1} need to prevail. For the geometries in the chamber, we can see that Reynolds numbers of maximum Re 20 occur on the outer wall and Re 3.7 on the micropillars. Compared to the theoretical transition for walls of Re 150000-1500000 Re (Sforza, 2014) and for pillars of Re 300-30000 (Sunden, 2008), it is evident that there is no turbulent flow in the microfluidic cell. In the chamber, the velocity would theoretically have to be at least 8 m s^{-1} to achieve turbulent flow. Also, upon closer examination of the fluid flow around the posts, it is apparent that no Kármán vortex effects are created, as this occurs at Reynolds numbers of approximately Re 40-90 (Sunden, 2008).

3.6 Wall shear forces and velocities on micropillars

An essential part of the fluid flow and bacteria adhesion assessment in the cell, is the consideration of the micropillars and their effect on the fluid. Therefore, the next step was to visualize how the fluid behaves at the micropillars. In addition, the occurring wall shear forces were measured at the micropillars and displayed graphically.

3.6.1 Formation of oval velocity lows on the microfludic cell

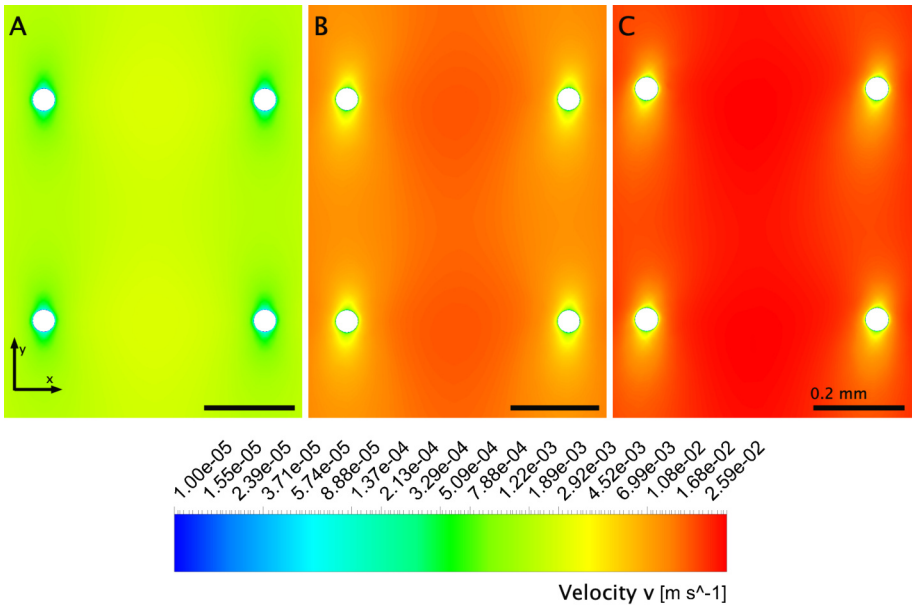

FIGURE 3.7: **Contourplot of velocities in micropillar region** . The three different velocities **(A)** 1 mm s^{-1}, **(B)** 12.5 mm s^{-1} and **(C)** 25 mm s^{-1} are shown in logarithmic color scale. The image is enlarged and shows four micropillars in 2x2 formation in the center of the chamber section. The fluid flows from top to bottom. Exact location of the detail in 2.2

.

In figure 3.7 it is evident that at all three simulations, the velocities and thus the fluid flows, slow down around the pillars completely and in addition

form an oval fluid region with low velocities in the direction of the flow above and below the pillar. This behavior is visible at each of the three velocities. Comparing figure 3.7 **A** with figure 3.7 **C** it can be seen that the oval region becomes more inclined in x-direction as the velocity increases. The same pattern is visible between figure 3.7.**A** and 3.7.**B** but it is not as pronounced. If the y-direction of all simulations between the micropillars is considered, it can be seen that although there is a flow, it is strongly attenuated and forms a region between the micropillars in the fluid direction with medium velocities. The highest velocities can be detected horizontally between the micropillars in the x-direction.

3.6.2 Uniform wall shear forces around the micropillars

Next, the occurring wall shear forces on the micropillars were determined and visualized to complement the previous graphical analysis.

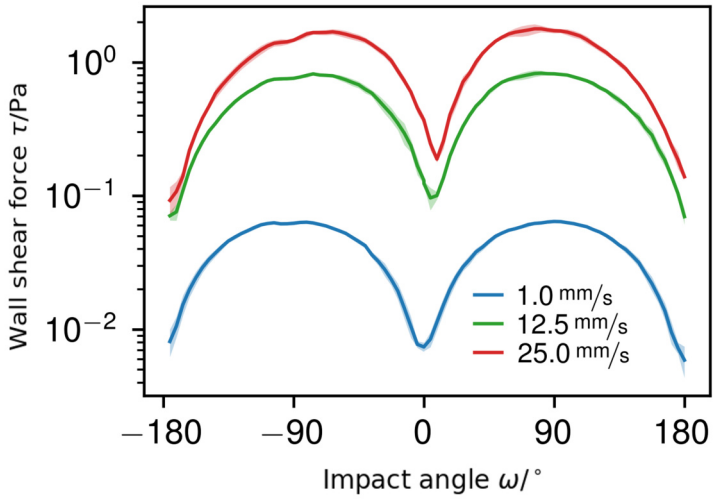

FIGURE 3.8: **Wall shear stress on micropillar in the middle of the cell.** Mean wall shear forces on the micropillar at varying velocities with a logarithmic y-scale. Shown is the mean and standard deviation of the micropillars in section 2.2 of the cell. The degree scale applied to a micropillar in 2D representation and starts with positive degrees in clockwise direction.

Figure 3.8 shows us that at an average cell velocity of $1\,\mathrm{mm\,s^{-1}}$, the wall shear force is highest at -90 ° and +90 ° and lowest at 0 ° and 180 ° . Thus, the wall shear force is as expected inversely proportional to the velocity incident in y-direction on the micropillar. At $12.5\,\mathrm{mm\,s^{-1}}$ and especially at $25\,\mathrm{mm\,s^{-1}}$, we see that the increase in velocity and displacement of the fluid flows in the right part of the cell, as already seen at section 3.4, results in a displacement of the incident wall shear force. This can be seen in the figure 3.8 by a slight shift of the maximum shear forces outside the point + and - 90 ° degrees occurs.

3.7 Fluid flow and the occurrence of secondary flows

2D analysis is partially limited in the assessment of fluid flow mechanisms. To generate further insight from the flow in the chamber area, the geometry was simplified and subjected to 3D simulation. In the following section, the fluid flows in the 3D simulation are shown qualitatively.

3.7.1 General flow behavior and acceleration at the micropillars

In a first step, a contour plot of the velocity in the chamber was used again to create a general understanding. The general understanding is pertinent to understand the later step of secondary flow analysis.

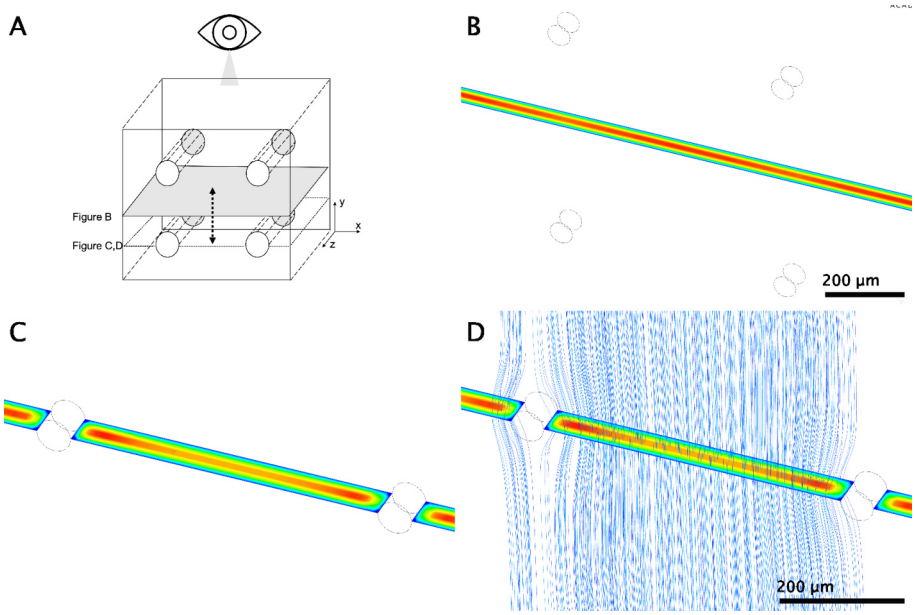

FIGURE 3.9: **Velocity contour plot of 3D chamber section.** color scale selected locally in z-plane. Red color indicates high velocity, blue color indicates low velocity. **(A)** Illustration of the cutout and locations of the displayed plots. **(B)** Qualitative velocity plot with plane created in the middle between the micropillars in y-direction (y = 250 μm). **(C)** Qualitative velocity plot with local velocity scale in z cutout plane. Plane selected in center and between two micropillar. **(D)** Additional visualization with streamlines on same location as in **(C)**. Streamlines neutral, without velocity gradient.

As expected, we see in figure 3.9.**B** that the flow slows down at the outer walls and fully forms in the center of the z-plane. From figure 3.9.**C** it can be seen that the flow between the columns does not have a uniform velocity, but is faster near the columns than in the center. Figure 3.9.**D** shows that the flow displaced by the micropillar is accelerated, resulting in an increase in velocity at the outer center. The fluid directly at the micropillar is completely decelerated. Figure 3.9.**B** shows us additionally the uniform developed and little influenced flow, in between the micropillar in y-direction.

3.7.2 Occurrence of secondary flows near micropillars

In the further course, with the knowledge of the general flow and the visualization of the flow in z-direction, secondary flows are analyzed.

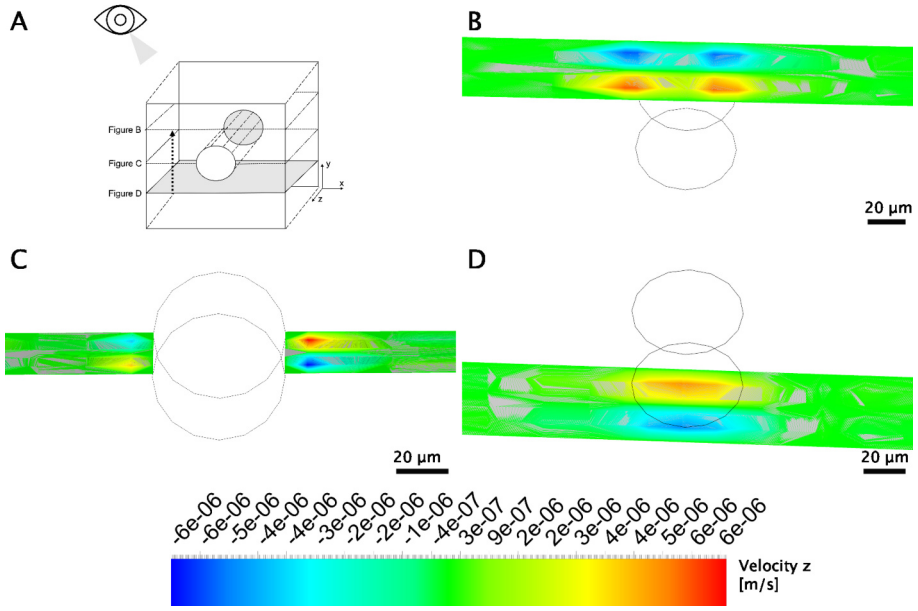

FIGURE 3.10: **Secondary flow around micropillar.** The velocity in z-direction is shown. The results are presented qualitatively. All images are taken from the simulation with the average chamber velocity of $1\,\mathrm{mm\,s^{-1}}$. Z-axis arrow drawn in the graph **A** shows positive values. Positive z-velocities (red) and negative velocities in z-direction (blue) are visible. **(A)** Illustration of the cutout and locations of the displayed plots. **(B)** z-plane above the micropillar. **(C)** z-plane in the middle of the micropillar. **(D)** z- plane below the micropillar.

Figure 3.10 shows that velocities in z-direction and thus flows in z-direction (secondary flows) occur near micropillars. The secondary flows as shown in the figure, occur consistently at each micropillar in the chamber and differ vary depending on how strong the flow is at height y in the microfluidic cell. It can be observed in figure 3.10.**B** that the velocity above the micropillar, i.e. at the point of impact, points towards the outer walls of the cell, which means that also the flow flows in direction of the outer walls of the microfluidic cell. Below the cell in figure 3.10.**D**, velocities are evident converging to the center of the cell. Thus, the fluid occurs towards the center of the cell. The same phenomena were observed in figure 3.10.**C** on the sides, where it is evident that secondary flow on the right side points to the center of the cell and the secondary flow on the left side, to the opposite. This phenomena occurs exactly at the transition between the upper and lower half of the pillar.

3.8 Correlation between fluid flow and bacterial growth

In a final step, an image analysis of the cellulose concentration in the experiment 2.1 was performed to investigate how the Biofilm and EPS was formed

in the context of previous bacterial growth analysis and whether a connection with the flow behavior in the system, respectively with the previous analyses, is observable.

3.8.1 Possible biofilm displacement, due to fluid flow shifting

In a last step, we analyzed the concentration of the biofilm and EPS in the four sectors 2.3 over a time of 100 minutes to find out if the simulated findings correspond to the real experiments.

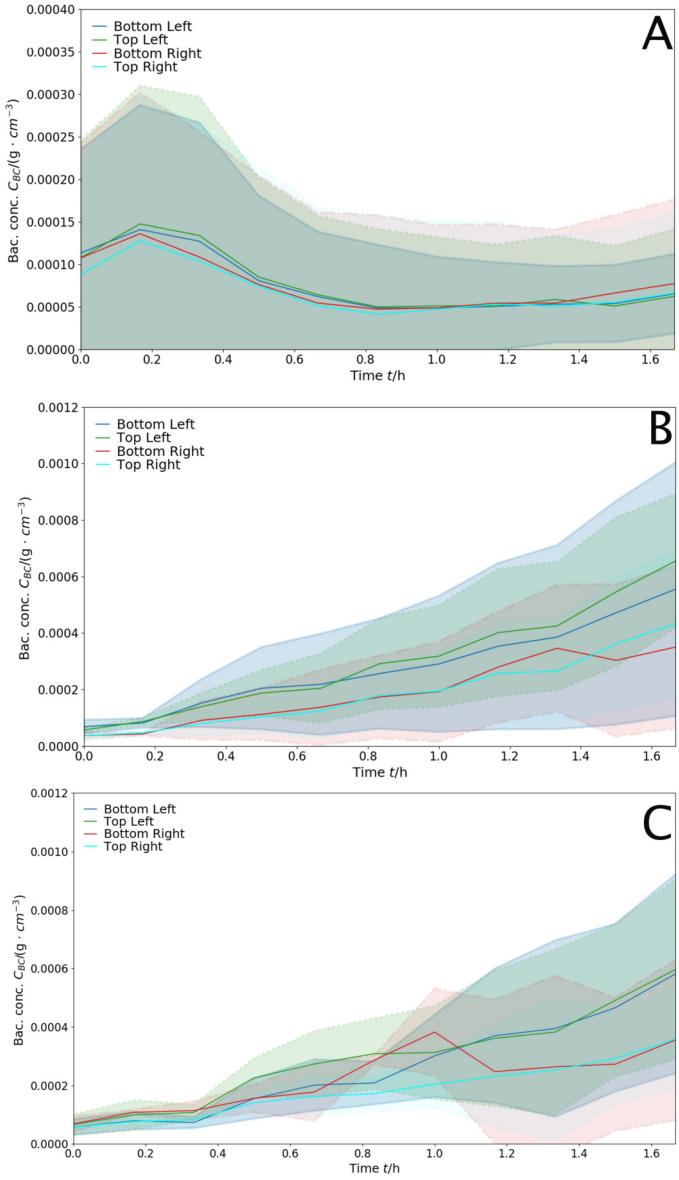

FIGURE 3.11: **Biofilm and EPS concentration analysis** Median of all experiments over 100 minutes. Divided into four sectors 2.3. In each case median absolute deviation visualized. Divided (Median and MAD) in Bottom left (*blue*), top left (*green*), bottom right (*red*) and top right (*cyan*). **(A)** First 100 minutes for 1 mm s^{-1} , **(B)** First 100 minutes for 12.5 mm s^{-1} **(C)** First 100 minutes for 25 mm s^{-1}

We see in figure 3.11.**A** that at a velocity of 1 mm s^{-1} there is no concentration difference in any of the cell sectors. The first apparent increase is due to an exposure error in the photograph. In figure 3.11.**B** and in figure 3.11.**C** we can see that after 100 minutes, there is a concentration difference between the left and right side of the cell. The concentration in the left side of the cell is higher. It is also evident that the median absolute deviation at all three speeds that the values overlap and so no clear statements can be made.
In the following table 3.6 the rise of the biofilm and EPS concentrations between the start and end point of the analysis can be seen. We can observe that with higher velocities there is a larger range between the concentration differences.

TABLE 3.6: **Concentration rise in the individual sectors**. The rise in concentration **CR** between the start and end points for each sector is shown (difference of end-and startpoint). Additionally standard deviation of the calculated differences.

Velocity / **Sector**	1 mm s^{-1}	12.5 mm s^{-1}	25 mm s^{-1}
	CR ($\frac{g}{cm^3}$)	CR ($\frac{g}{cm^3}$)	CR ($\frac{g}{cm^3}$)
Bottom left	$4.81e-05$	$4.87e-04$	$5.24e-04$
Top left	$4.53e-05$	$5.98e-04$	$5.30e-04$
Bottom right	$3.02e-05$	$3.13e-04$	$2.87e-04$
Top right	$2.17e-05$	$3.96e-04$	$3.01e-04$
Standard deviation	$1.26e-05$	$1.23e-04$	$1.35e-04$

From the table 3.6 it can be seen that the concentration differences between the start and stop of the measurement, for the systems with the velocities with 12.5 mm s^{-1} and 25 mm s^{-1}, are higher than for the system with 1 mm s^{-1} cell speed. In addition, for each system it is evident that the concentration increase on the right side (bottom and top), is lower than on the left side (bottom and top). At the higher velocities it can be seen that the top halves show a larger concentration difference, while at 1 mm s^{-1} it is the other way around. More relevant, however, is the standard deviation, which is higher in the faster systems and shows that the individual concentration differences are further apart.

Chapter 4

Discussion

Through the CFD analysis, we wanted to show both in the 2D and in the 3D visualization, which flow behavior the bacterial fluid exhibits in the microfluidic cell and thus, on the one hand, to identify geometric influences on the fluid, on the other hand, we wanted to gain further insights into the fluid dynamics of microfluidic cells and incorporate theoretical concepts of Biofilm and EPS formation.
We were able to observe how the geometry significantly affects the flow behavior of the fluid and clearly showed where the weak spots of the selected geometry are. In addition the analysis supports the theory of the formation of biofilm streamer due to the occurrence of secondary flows and the adhesion correlated with the wall shear forces. In the following chapter, the results are summarized and discussed.

4.1 Suboptimal geometry of microfluidic cell leads to significant change of fluid flow

When considering the general flow simulations at $1\,\mathrm{mm\,s^{-1}}$ (figure 3.3), i.e. with optimal flow properties in the microfluidic cell, it becomes apparent that the geometry in the lower chamber plane on the bottom left and bottom right at the wall (3.4) is not optimally flowed through and is accelerated by the suction of the outlet towards the center of the chamber. This results in EPS orientation in the lower part of the cell that is not aligned in a straight line, which can lead to negative effects in the subsequent mineralization process. The behavior indicates that there is no uniform flow in the lower part of the cell and therefore, there is a geometric misconstruction. This incorrect design can be due to the fluid inlet but also to the outlet area. It is assumed that the geometry of the outlet area in particular leads to a suction effect, since there is only one channel for discharging the fluid. We have seen in the examination of the experiments (3.2) that the same effect of diagonal EPS formation, occurs in the lower part of the microfluidic cell for all velocities.

With additional inclusion of image analysis, there was no difference in EPS concentration between the lower part of the cell and the upper part of the cell observable, which indicates that the suction of the outlet has no quantitative influence in biofilm growth. Means that the microfluidic cell is flowed through at an inclination and thus EPS is still formed as in the upper half of the cell. However, in contrast to the upper part of the cell, an optimal layer

structure is not achieved. This is of relevance, since for the later work in mineralisation the layer structure needs to be as parallel as possible. In order to eliminate the deficiencies at the geometry, different modifications could be carried out. The outlet area could be redesigned to reduce the suction effect on the fluid. For example, instead of one large outlet channel, several smaller outlet channels or a bifurcated outlet similar to the inlet could be created. Various examples from medical technology, such as the Osteogenesis-on-a-Chip Microfluidic Device from Bahmaee et al., 2020 or a Single Cell Trapping Microfluidic Device from Weng et al., 2016, show that more constant fluid flows can be achieved by multiple outlet channels in the lower region of the cell.

We have observed with the help of the velocity increase simulations in the microfludic cell, that due to the increase of velocity in the system, there is an increase of velocity in the right part of the cell and therefore, a fluid mass displacement is suspected. There is not only an increase in velocity in all channels but in particular an increase in velocity in channels 9, 13 and 16. The shift is caused by a suboptimal design of the inlet. Due to the current construction, the fluid does not hit the first separator of the microfluidic cell perpendicularly and is thus disproportionately led into the right area of the cell. Looking at the velocity measurement in the center of the cell, we have seen that the velocity peaks have evened out, but still predominate on the right side of the cell. To confirm this fluid shift, in a further step we observed the initial bacterial growth in the individual cell areas during the first 100 minutes (3.8.1). We have seen, that when the velocity is raised, the concentration buildup is higher in the left part of the cell (BL, TL). The reason for the slower concentration build-up of the right part, is that when the velocity is increased, a proportional increase in the shear forces on the micropillars is generated, which affects the adhesion of the bacteria to the micropillars 4.3. Due to the small number of experiments, there is a high standard deviation and a high uncertainty of the analysed concentration increases, which must be taken into account. We see that the median of the data suggests an initial shift of the fluid to the right and thus an initial shift of the bacteria formation in the right part of the cell, but we cannot confirm it because of the high uncertainty. In addition, the redistribution of the fluid flow could increase the likelihood of creating a non-linear flow, leading to chaotic excretion of EPS described in chapter 4.2.

If we look at the concentrations over the entire test period, we cannot see any clear final concentration differences in correlation with the increase in velocity and the inclined inlet. This is explained by the fact that the increase in concentration in the cells simultaneously creates a dynamic fluid flow, since the differences in concentration create pressure differences that cause the fluid to be displaced in the cell depending on how large the obstacle is on the particular side. However, it should still be considered that it is likely that the irregular flow could lead to clogging in the cell as described from Valiei et al., 2012. The results confirm the processes described from Stoodley et al., 2007.The dynamic processes in the cell, were not considered by the simulation and therefore cannot be described.

To improve the geometry and therefore make the fluid flow in the microfludic cell more uniform, a simple straightening of the first inlet can be done. The effectiveness of such a bifurcation inlet has already been seen in Davydova et al., 2016 and also simulated from Liu, Li, and Lew, 2010, and can be achieved with minimal effort. In the approximation with an additional simulation with modified geometry in appendix A, we have seen how the fluid behaves when the first inlet is straightened. It can be seen that at high velocities, the previous peaks disappear and new peaks appear at outlets 1 and 16. However, the general distribution is more uniform and leads to a more orderly fluid flow, as Liu and Li, 2013 has already described. In addition, the straightening due to the higher velocities on the outside results in a better flow on the outer sides and improves the problem of missing EPS formation in the lower corners. The additional simulation was carried out without a detailed examination of the network and can therefore not be included as a result.

From a geometrical aspect, we can conclude, that the analysis showed two major problems that are most likely due to the incorrectly designed geometry and need be improved in order to to create a uniform fluid flow inside the microfluidic cell.

4.2 The increase in speed leads to problems in biofilm and EPS production.

We have seen that the increase in speed has resulted in a faster EPS concentration rise in the system (3.1), as already discussed in the study of Valiei et al., 2012. The reason for the faster biofilm buildup at higher fluid velocities is presumed to be in the higher probability of bacterial adhesion and cohesion because of the larger number of organisms that flow into the microfluidic cell. At the same time, we can see that a maximum of the ratio of cellulose formation and velocity increase, occurs. This maximum can be explained by the increase of the wall shear force on the micropillars and thus the impossibility of adhesion of the bacteria, since the adhesion force is no longer sufficient for the adhesion to the walls. Also in the studies of Valiei et al., 2012 we see that the excessive increase in velocity, leads to a plateu in biofilm formation and even, the biofilm formation can be stopped completely by washing away the transverse biofilms. In the study of Valiei et al., 2012 they used a maximum velocity flow rate of: Q_{max}= 0.022 μl s^{-1} (in study: Q_{max}=11.25 μl s^{-1}), which has led to transverse biofilm streamers but no permanent streamer formation. It should be mentioned that the study worked with a geometry that had distances between micropillars 20 times smaller than the used cell in the study. The exact point where velocity led to biofilm degradation has not been determined in Valiei et al., 2012 or in the study performed. The results are relevant because by accurately determining the velocity, the buildup of biofilms in microfluidic cells can be optimized to build up as quickly as possible with as little loss of EPS as possible. In addition, the lower velocity in the microfluidic

cell ensures that biofilm formation occurs in a more controlled manner, which will be discussed further in the text. Therefore, for the optimization of the microfluidic cell, it is recommended to find out the optimal point empirically. It should be noted that this point is geometry dependent and not applicable for every system. Nevertheless, the results should be viewed critically, since the number of experiments amounts to four experiments per velocity and thus not enough data is included.

Contrary to the hypothesis that turbulent flows could be generated by the velocity increase, no evidence was found by the analysis. In the theoretical calculation, we have seen that the applied velocities, in any geometry (3.5), did not lead to exceeding the critical Reynolds numbers. Theoretically, the velocities would have to approximately 90 times higher to reach this critical point. Also, the potential occurrence of a Kármán vortex flow behind the micropillars could be excluded by the calculation of the Reynolds numbers.The knowledge that there are no turbulent flows or a Kármán vortex street in the system allows on the a simpler and more accurate calculation in the CFD computation and also it is at same time advantageous for the real microfluidic cell. It can be excluded that the velocity increase, in the cell leads to three-dimensional flow fields, which would lead to significant consequences in the formation of laminar EPS structure, since the biofilm formation would be disturbed by cross flows and thus no linear EPS structures could develop. The formation of laminar structures in the microfluidic cell, serves as the core idea of the project and would make the continuation impossible. Laminar flow in microfluidic cells, was already described by Rusconi et al., 2011, which assumed laminar flow with $\mathrm{Re} \sim 1$, Valiei et al., 2012 with $\mathrm{Re} \sim 0.01$ and also can be confirmed by the analysis. It should be mentioned that the Reynolds number can only be determined empirically and is therefore not exactly matched to the geometry present in the investigation. In order to determine the geometry-specific critical Reynolds numbers, further measures were taken or would have to be taken, which are described in the next section.

Since the Reynolds calculation and experience from other studies showed that no turbulent flows appeared at the selected velocities, the Reynolds calculation was not continued. Nevertheless, there are possibilities to determine the critical Reynolds number with CFD. For a simpler but not sufficiently accurate determination of the critical Reynolds number, the velocity would have to be adjusted around the theoretically determined critical point and increased. The analysis needs to be done in a transient simulation.Then, either examining the flow field for turbulence intensity, or doing a spectral analysis of the velocity fluctuation to detect turbulence could be used to detect 3D-flow fields. By this method, turbulence could be captured and provide the approximate transition range from laminar to turbulent, but not exactly determined. The biggest limitation in finding the critical Reynolds number, however, is the grid fineness that must be high to detect turbulence. The turbulence models only give methods to approximate turbulent flows, but cannot provide enough data to determine the critical Reynolds number. Therefore,to determine accurate critical Reynolds numbers, a direct numerical simulation

(DNS) would have to be performed, which means that no turbulence model is applied and thus very fine grids are generated and high computer power is required (J. and M., 2008). Considering that the velocities to be determined for the critical Reynolds number would be approximately $8\,\mathrm{m\,s^{-1}}$ for the system, the execution of simulations (or experiments) with these velocities would not be feasible at all, since the cell would not withstand the resulting pressure and a total shift of the fluid flow would occur in the simulation, the execution of a DNS and thus the determination of the critical Reynolds number for the whole microfluidic cell, does not make sense. In addition, the execution is not possible for resource reasons. The only possibility that is predictable and makes sense is to determine the critical Reynolds numbers on specific geometries. For this, all prevailing geometries would have to be analyzed individually in different DNS.

By looking at the concentration rise over the whole cell (3.1), it is evident, that EPS formation in the systems with higher velocity, is more random and can be classified as unpredictable. This behavior is also qualitatively evident from the experience in experiment execution and the analysis of the experimental EPS growth images obtained with figure 3.2. These random EPS structures are often characterized by the formation of transverse biostreamers or the non-straight biofilm deposition. This can be explained by the fact that the high velocity does not create a transition into the turbulent region, but increases the kinetic fluid energy, which by impacting on the walls, creates fluid flows, in a undesired direction, which prevents the straight-line formation of biofilms by interrupting biofilm formation processes or directing them in an undesired direction of formation. Additionally, as already described in chapter 4.1, the unfavorable geometry in the system leads to an increase in the non-uniform flow into the chamber, and thus, increases the velocity at specific points, which leads to an enhancement of the effect described above. We have observed this effect well for increased velocities ($12.5\,\mathrm{mm\,s^{-1}} \leq \mathrm{V}$) in the simulation 3.5. Another source of unstructured flow is the sensitive system itself. Very small particles of sand or fibers, are deposited in the cell and are difficult to remove, causing the fluid to be discharged and again leading to chaotic EPS formation. One possibility to minimize these undirected flows could be the change of geometry mentioned in chapter 4.1. The change of geometry would lead to a more rectilinear flow into the chamber area on the one hand and to a more straight flow out of the chamber area on the other hand, which would lead to a minimization of the unwanted undirected flow at higher velocities. The evaluation of the quality of the EPS formation is difficult, because on the one hand the number of experiments is insufficient for a definitive statement and on the other hand, a approriate tool for the evaluation of the cellulose structure in the microfluidic cell is needed. How the formation of transverse biostreamers in the system is related to the formation of chaotic strucured EPS was not assessed.

In summary, we have observed that velocity is directly correlated with the buildup of biofilms in the cell. However, if the shear forces acting on the micropillars exceed the adhesion forces of the microorganisms as the velocity

increases, less biofilm is formed or degraded. We have shown that the velocity in the microfluidic cell does not lead to turbulent flow, but due to impurities, single velocity peaks, too high velocities and geometric errors, unstructured EPS deposits are formed.

4.3 Adhesion and rheotaxis of microorganisms at micropilllars

In order for biostreamers to form, the first step for the microorganisms is the biofilmformation to the micropllars. As seen from Vasudevan, 2014, this happens through the initial adhesion of the microorganisms to the micropillar. From Das and Kumar, 2014 and Valiei et al., 2012 it was shown that the initial adhesion to the micropillar occurs around the whole micropillar, but some areas above and below the micropillar are characterized by a stronger agglomeration of biofilm. From the simulations on the micropillars we know that the lowest wall shear forces occur above and below the micropillars (0 ° and 180 °) and the highest on the sides (90 ° and -90 °). This behavior was also shown by Hassanpourfard et al., 2015. Since we see a clear correlation between inital biofilm formation and shear forces, we can therefore observe, as expected, that the shear forces control initial biofilm production in that adhesion to the micropillar occurs, but cohesion forces on the sides of the micropillar are often insufficient to counteract the shear forces. Thus, initial biofilms predominantly accumulate on the top and bottom of the micropillars. At further increasing velocities, as seen in figure 3.1, a point is reached where cellulose generation no longer correlates with increasing velocity and the the shear forces that occur exceed the adhesion forces and lead to the degradation of biofilm on the sides of the micropillars.The level of adhesion depends on various mechanisms acting on the adhesion force, with hydrophobic interactions dominating. Mechanisms that are controlled by the specific composition of the biofilms are. We see that the uniform flow through the fluid and the application of uniform wall shear forces are the basis for the network-like structure formation of biofilms. This rather simple and expected biofilm agglomeration, is essential for the further biostreamer formation between the micropillars, because the structured arrangement of the biofilms around the micropillars determines in the further course whether the biostreamers also take a structured form. In order to generate a more efficient initial formation of the biofilms, the shear forces could be determined at which the biofilm adhesion is exceeded. The results of the wall shear stress, cannot describe the streamer formation and only indicate where the primary adhesion takes place.

From the observations of the velocity increase in the chamber region (3.5)) we have seen that with an increase in velocity, shifted wall shear force peaks appear. These shifts indicate an uneven force distribution in the micropillar region and in combination with the knowledge of the initial bacterial adhesion, suggest the formation of uneven biofilm agglomerations. This leads to an impaired biostreamer formation in the next step and to a disruption of the

network formation by formation of nonlinear EPS formations. As allready described in chapter 4.2. We know from Valiei et al., 2012 that structured biofilm formation depends strongly on the fluid velocity. If the velocity is low, the bacterium is deposited everywhere in the cell and no ordered biofilms are formed, if the velocity is too high, we see that biofilm streamer are formed quickly and also in transverse flows, but it is washed away again due to the high shear forces.

Since the velocity in the CFD simulation shows inversely proportional behavior to the shear forces, we could observe that when comparing the contour plots in figure 3.4 and initial bacterial adhesion or biostream formation clear correlations can be seen, between low velocity areas occurring and biofilm agglomeration and development location for the first biostreamers. The velocity contour plots in the chambers, show that around the posts at the point of impact and parallel on the 180 ° side, slowed fluid flow areas form in an oval shape. Compared with the experiences and pictures of the experiments and from the studies of Das and Kumar, 2014, we can conclude that exactly these slowed down areas become apparent as the first areas with a recognizable biofilm formation. This therefore means that velocity can be used as an indicator to detect areas of potential adhesion and biofilm streamer formation. However, it should be noted that this appears to be valid only for the initial phase and linear flow in the microfluidic cell, since in the course of streamer formation in the cell transverse streamers appear and invalidate the correlation.

Looking at the streamer formations, in the microfluidic cell, we see both, in the analysis, as well as already evident from studies (Das and Kumar, 2014; Valiei et al., 2012), that the initial streamer formation appears to occur at points 0 ° and 180 ° of the microfluidic cell. In conjunction with the wall shear force, we know that these points at the same time, are responsible for a stronger agglomeration of biofilm. In addition, we have observed that secondary flows are generated near the micropillars and that they flow against the wall or converge into the center of the cell, depending on whether they are above or below of the micropillar. As already simulated and observed from Valiei et al., 2012. Based on the hypothesis that secondary flows are a mechanism of in biostreamer formation in microfluidic cells and the findings of different studies (Rusconi et al., 2010; Rusconi et al., 2011; Drescher et al., 2013), that showed biofilm formation in curved channels as a result of secondary flow, we can see that the relationship between biofilm streamer formation and location of secondary flow occurs in a first phase. The first biofilms formed, as also seen in (3.2), can all be seen below the microfluidic cell. At the location below the microfluidic cell, the simulation has revealed secondary flows converging towards the center of the cell. Additionally, we know that there are no turbulent flows in the system. The findings, by comparing, with the findings from Rusconi et al., 2010, show that the same phenomena becomes observable. The formation of biostreamers seems to be controlled by the secondary flow. In a second, more developed phase of biofilm formation, we see that transverse streamers are also formed. In this phase, it is not possible

to identify the secondary flow as the driving force in the biofilm formation, since the simulation is not dynamic and assumes an EPS-free cell. In addition, we know that transverse biofilms are formed due to the increase in velocity in the cell, thus allowing the statement of the correlation between secondary flow and biofilm formation only under certain conditions. However, it is still suspected that the secondary flow plays an important role in the formation of biofilms.

Since we know that the increase in biofilm production is strongly correlated with the increase in velocity, it is believed that the biostreamer formation in small Re< 1 are a product of the viscoelastic properties of the biofilms and the occurring flow in the cell, supported by the secondary flows in the cohesion of the biostreamer. The viscoelastic biofilms are deformed by the flow and by the occurrence of shear forces. The occurrence of secondary flow supports the biostreamer formation, by guiding the streamers through the flows of the secondary flow converging into the center in such a way that they preserve the biostreamer shape. Increasing the velocity therefore leads to more biostreamers, because a greater shear force results in a larger faster and higher deformation. How the biostreamers adhere to the next micropillar and whether the occurrence of secondary flows plays a role is not clear and remains ambiguous.

In conclusion, we have seen that the fluid flow is responsible for both the positioning of biofilms and the formation of biostreamers. The fluid velocity and the resulting phenomena are responsible for the control. In combination with the structured micropillar geometry, no biostreamer structures form at low velocities or uncontrolled biostreamer structures form or are carried away at high velocities. The adhesion behavior in the network formation shows the same processes as in the experiments on single micropillars.The rheotactic behavior of the microorganisms on the micropillars, on the other hand, still shows many uncertainties in the formation of biostreamers in network structures. All in conclusion, it is assumed that the rheotactic formation of biostreamers is subject to a combination of different hydodynamic processes and should be investigated in further studies.

4.4 Verification and Validation of the simulation

A distinction can be made between verification, which is mostly covered in chapter 3.2 and validation, which is covered in this chapter.
We assume that the boundary conditions are adjusted to the system and have seen that the quality of the mesh and the mass balance meet the requirements to generate a sufficiently accurate solution for the problem definition. In addition, we know from the simulation that the convergence criteria have all been met.(Oberkampf and Trucano, 2002)

From the results of the pressure validation process, as described in **??** we have seen, that the pressure difference from the simulation, at an average chamber velocity of 25 mm s^{-1}, between the inlet and the outlet is 0.1869 bar. The pressure based validation, performed at the same velocity, showed 0.081 $\pm$0.00192 bar. The offset of the measuring device of 0.034 bar has already been taken into account. So we have 0.1059 bar difference between the simulated and real value. To understand why the difference is so high and why this value can still be used as a validation, we need to take a closer look at the analysis since the difference may be caused by several factors. The first important reason for the inaccuracy is the pressure gauge (CPS 2184 Z, 5 bar, CETONI, Korbussen, Germany), which is not suitable for accurate measurements at such pressures, since the membrane pressure gauge is designed for pressures from 0.5-600 bar and our experiment always takes place under 0.5 bar. This means that the error calculation with the manufacturers data sheet is not possible at all and additional errors of unclear dimensions must be expected. Another reason is the correspondence between the real speed prevailing in the system and the calculated speed. The real velocity is given by the setting in the syringe pump, while the calculated velocity in the inlet is calculated from a velocity to be reached in the cell. The calculation contains errors in the unclear geometry-related conversion and the inaccuracies of the density measurement of the fluid. The last important point for the inaccuracy between the two values is the scraped out cell. The scraping of the cell is done manually and should ideally be 50 micrometers deep. However, since this was not possible, deeper and less deep spots were created, which caused pressure differences.In addition, the cell with the inlet area was scraped out. The unnecessary scraping of the inlet area leads to a reduction of the pressure in the system and affects the measurement,as the measured pressure decreases. With all factors considered and the knowledge that the validation range is at a low pressure level with values that are difficult to determine, the simulation was nevertheless classified as validated. Nevertheless, to allow a more accurate validation, a more accurate measurement must be performed. In principle, this can be done in such a way that the points discussed earlier are improved. That implies that a pressure gauge for lower pressures must be used and that a microfluidic cell with a cleanly scraped interior needs to be designed. The calculated velocities should be checked again and corrected if necessary.

As additional validation supplementary, respectively confirming to the pressure validation, the concentration analysis was selected (2.5.2). The velocity shifts to the right side calculated in figure 3.11 could be made evident by the concentration analysis. The median of the measurement series does show us the behavior that we expect (lower concentration on the right side). The fluid flow shifted by the simulation and the concentration difference in the cell halves determined in the image analysis, therefore, show that the simulation and the real values seem to correlate. It must be noted, however, that the overlapping standard deviations in the concentration analysis are subject to uncertainty and thus, no comprehensive validation can be achieved with the concentration analysis. The limitation in the measurement series leads to

the fact that on the one hand we could have a falsified median because the number of measurement series is too low and on the other hand that our variance overlaps in all sectors and so the confirmation is not possible.

In addition, due to the dynamic behavior of bacterial growth, a statement based on the static simulation is only possible to a limited extent. The simulation represents the cell without EPS deposition and can therefore only represent a certain time in the simulation. Overall, the validation only via the concentration analysis is therefore not sufficient. To enable the validation via the concentration analysis, the number of measurements has to be increased. In addition, a dynamic simulation could be created that represents the EPS growth.
Even if the validation via the concentration measurement and the pressure measurement is partially subject to errors, the combination of the two validation options and the still rather positive results enable us to validate the simulation. A further improved validation is explicitly recommended.

Chapter 5

Conclusions and Recommendations

5.1 Conclusions

We have simulated a microfluidic cell to analyze the existing fluid flows and to derive conclusions of the geometry and rheotaxis of the microorganism culture. In doing so, we were able to gain insights into both the geometry and the general understanding of microfluidic flows.

We have observed that the geometry can be improved at the inlet and outlet section to ensure a more uniform fluid flow and thus a more structured and uniform EPS-concentration in the cell. The current geometry indicates that the fluid enters the chamber unevenly and causes shifts in the distribution of the bacterial fluid. Also the general distribution of the fluid, is not optimal due to the current design. Additionally, we have seen that the velocity in the cell is often too high for the actual geometry and results in an uneven and non-uniform EPS expansion. The resulting problems in the fluid distribution, is a combination of geometry and increased velocity and can be improved by velocity optimization in addition to geometry change, so that the EPS concentration buildup is at a maximum.

In terms of general understanding of the microfluidic flow, the analysis showed how the fluid behaves in the inlet area, chamber area and especially around the micro pillars. By analyzing the wall shear forces, we have seen that we can identify where bacterial adhesion potentially works best and how this relates to biofilm formation, as described in section 4.3. In terms of biofilm formation, can we conclude, that the occurrence of secondary flows, on the initial biofilm production a connection with the formation of these is suspected. The results of the study together with the findings of Rusconi et al., 2010 indicate that rheotactic biofilm formation is a combination between secondary flow theory and viscous fluid theory.

5.2 Recommendations

5.2.1 Geometry

The geometry should be optimized in the inlet and outlet area. It is especially recommended to redesign the inlet area, because this is the easiest solution to create more uniform fluid flows and at the same time to close the EPS gaps at the lower corners of the cell. How the fluid movement improves could be illustrated in a approximate simulation seen in Appendix A.To optimize the geometry further, the outlet area could be redesigned so that multiple outlet channels minimize the suction effect. In addition, the optimum velocity for the geometry should be determined. This must be high enough to still ensure a guided fluid movement in the cell and maximum adhesion of the bacteria to the chamber walls and micropillars.

5.2.2 Simulations

In order to obtain better and additional results, the simulation could be extended in various areas. The most relevant change would be to increase the number of possible cells to generate high quality 3D simulations of the complete cell. The extension of the cells could provide a more detailed view of all fluid dynamic problems in the 3D geometry. An even more accurate simulation, could be generated by a direct numerical simulation (DNS) of the cell. The DNS would allow to determine the critical Reynolds numbers of the cell and also to visualize more complex fluid flows around the pillars.

In order to simulate the dynamic biofilm growth, further simulations with modified geometries could be performed. Based on the experimental images, the geometries could be changed in such a way that biostreamers would be considered rigid at certain points in time. These rigid sites would simulate the biofilms and thus better represent the dynamic processes. With the increase of simulations and geometries, the accuracy of the dynamic simulation would also increase.

The entering liquid was assumed to be homogeneous in the simulation, but in reality it can be seen as a heterogeneous mixture of water and particles (bacteria in the biofilm). In order to simulate these conditions and to detect the deposition of particles at micropillars or other locations of the geometry, further simulations could be made visible with a paricle simulation.

5.2.3 Validation

Validation needs to be improved to clearly confirm the simulation. To achieve this goal, the pressure measurement must be done with a more accurate pressure gauge. Since the pressure gauge is currently only designed for pressures of minimum 0.5 bar, the accuracy cannot be guaranteed.In addition, a new geometry should be created for the measurement purposes, which does not have a micropillar structure, in order to avoid errors that occur when scraping the geometry. In addition, by increasing the number of experiments for

all three velocities, it could be confirmed via image analysis whether the fluid flow results in a shift to the right half of the cell as in the simulation.

In case of a geometry change and the increase of the number of channels, the mass flow, could serve as an additional possibility of validation. The mass flow of the real experiment could be measured in the outlets and compared with the simulation. The measurement of the mass flow would produce the most accurate validation method.

Appendix A

Additional simulation

A.1 Straightening of the inlet and the resulting flow

We have seen the fluid displacements indicated by the simulation due to the inclined inlet area. In order to minimize the resulting problems, such as the uneven EPS formation, a simple geometric change was made in an additional simulation in an attempt to improve the geometry. The inlet area of the existing geometry was redesigned in such a way that the inlet meets the first separator in the system in a rectilinear manner, thus eliminating the rightward displacement. The simulation is located in the Appenix, since this was not part of the investigation. In addition, the problem is that the simulation has many uncertainties and therefore a statement is only possible to a limited extent.

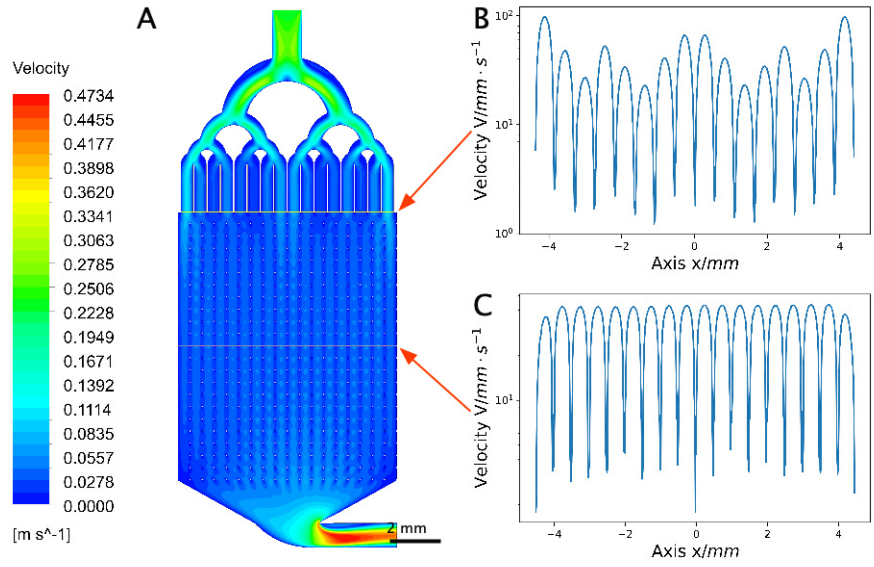

FIGURE A.1: **Straightening of the inlet** The inlet velocity selected is 25 mm s^{-1}. Both velocity graphs (**B and C**) show same measuring locations as in figure 3.6 and have both a logarithmic scale in y-axis. (**A**) Entire microfluidic cell with linear colour scale. Inletsection modified. (**B**) Velocity shown in inlet of chamberarea. (**C**) Velocity shown in the middle of cell.

In the figure B.2.**A** we see qualitatively that the straightening of the inlet at 25 mm s^{-1} still leads to an uneven shift of the fluid distribution despite the

improvement. The analysis of the graph B.2.**B**, confirms the unequal fluid distribution. As in the simulation (3.6), we see that velocity peaks occur at specific outlets of the inlets. However, note that unlike the simulation 3.6, inequalities arise, but they occur equally on both sides. The examination, from B.2.**C** shows the importance of this symmetrical inequality distribution, as we see that in the center of the chamber, as in simulation 3.6, there is a flattening of the velocity peaks. In the simulation with slanted inlet, however, we see a slight redistribution of velocity to the right side, even in the center of the chamber, which is not the case in the new simulation.

The finding that the straightening of the inlet does not produce a uniform flow, but a symmetrical imbalance, is relevant, because we see that in the center of the cell, no more velocity gradients arise and thus a more uniform flow can be produced. The more uniform flow results in less one-way plugging and more uniform EPS formation.

Appendix B

Supplementary Figures

B.1 Navier Stokes equation

- Mass conservation

$$\frac{\partial \rho}{\partial t} + \nabla \cdot \vec{m} = 0 \tag{B.1}$$

- Momentum conservation in x direction

$$\begin{aligned} \frac{\partial}{\partial t}(\rho \cdot u) + \frac{\partial}{\partial \cdot x}(\rho \cdot u^2 + p - \tau_{xx}) + \frac{\partial}{\partial y}(\rho \cdot u \cdot v - \tau_{yx}) \\ + \frac{\partial}{\partial z}(\rho \cdot u \cdot w - \tau_{zx}) - \rho \cdot g_x = 0 \end{aligned} \tag{B.2}$$

- Momentum conservation in y direction

$$\begin{aligned} \frac{\partial}{\partial t}(\rho \cdot v) + \frac{\partial}{\partial \cdot x}(\rho \cdot v \cdot u - \tau_{xy}) + \frac{\partial}{\partial y}(\rho \cdot v^2 \cdot p - \tau_{yy}) \\ + \frac{\partial}{\partial z}(\rho \cdot v \cdot w - \tau_{zy}) - \rho \cdot g_y = 0 \end{aligned} \tag{B.3}$$

- Momentum conservation in z direction

$$\begin{aligned} \frac{\partial}{\partial t}(\rho \cdot w) + \frac{\partial}{\partial \cdot x}(\rho \cdot w \cdot u - \tau_{xz}) + \frac{\partial}{\partial y}(\rho \cdot w \cdot v - \tau_{yz}) \\ + \frac{\partial}{\partial z}(\rho \cdot w^2 + p - \tau_{zz}) - \rho \cdot g_z = 0 \end{aligned} \tag{B.4}$$

- Energy conservation

$$\begin{aligned} \frac{\partial}{\partial t}[\rho \cdot (e + \frac{1}{2} \cdot \vec{u}^2)] + \frac{\partial}{\partial x}[\rho \cdot u \cdot (h + \frac{1}{2} \cdot \vec{u}^2) \\ -(u \cdot \tau_{xx} + v \cdot \tau_{xy} + w \cdot \tau_{xz}) - \lambda \cdot \frac{\partial T}{\partial x}] \\ +[\frac{\partial}{\partial y}[\rho \cdot v \cdot (h + \frac{1}{2} \cdot \vec{u}^2) - (u \cdot \tau_{yx} + v \cdot \tau_{yy} + w \cdot \tau_{yz}) \\ -\lambda \cdot \frac{\partial T}{\partial y}] + [\frac{\partial}{\partial z}[\rho \cdot w \cdot (h + \frac{1}{2} \cdot \vec{u}^2) - (u \cdot \tau_{zx} + v \cdot \tau_{zy} + w \cdot \tau_{zz}) \\ -\lambda \cdot \frac{\partial T}{\partial z}] - \rho \cdot (u \cdot g_x + v \cdot g_y + w \cdot g_z) = 0 \end{aligned} \tag{B.5}$$

B.2 Residuals

In the following example of defined and default residuals for a 25 mm s^{-1} Simulation with laminar turbulence system. The shown residual is just an example of three other defined residuals.

B.2.1 Example of defined residual

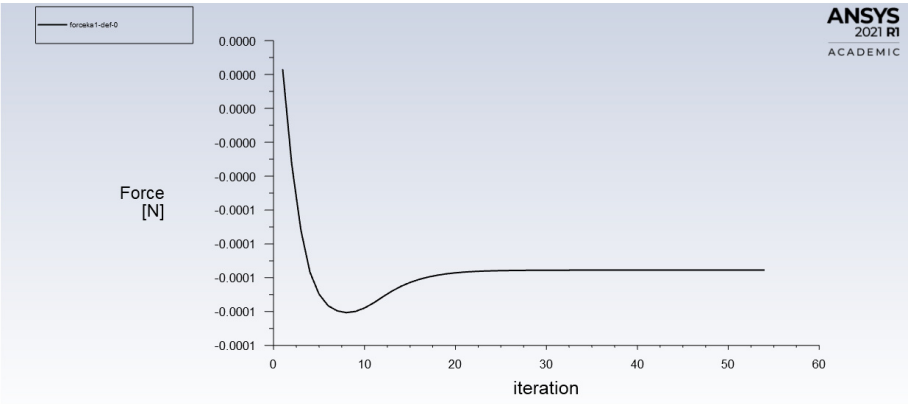

FIGURE B.1: **Defined Residual** Force on a micropillar defined as a residual.

B.2.2 Example of default residuals

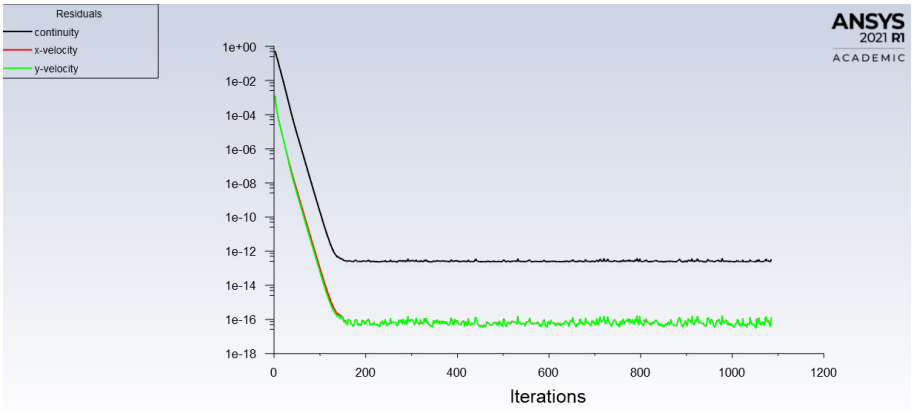

FIGURE B.2: **Default Residuals** Simulation is set with a laminar turbulence model and 25 mm s^{-1} chamber velocity.

Bibliography

Alfonsi, Giancarlo (July 2009). "Reynolds-averaged Navier-Stokes equations for turbulence modeling". In: *Applied Mechanics Reviews* 62 (4), pp. 1–20. ISSN: 00036900. DOI: 10.1115/1.3124648.

Aryasomayajula, Aditya et al. (2017). "Microfluidic Devices and Their Applications". In: *Springer Handbook of Nanotechnology*. Ed. by Bharat Bhushan. Berlin, Heidelberg: Springer Berlin Heidelberg, pp. 487–536. ISBN: 978-3-662-54357-3. DOI: 10.1007/978-3-662-54357-3_16. URL: https://doi.org/10.1007/978-3-662-54357-3_16.

Bahmaee, Hossein et al. (Sept. 2020). "Design and Evaluation of an Osteogenesis-on-a-Chip Microfluidic Device Incorporating 3D Cell Culture". In: *Frontiers in Bioengineering and Biotechnology* 8. ISSN: 22964185. DOI: 10.3389/fbioe.2020.557111.

Cheng, Zheng et al. (Nov. 2019). "Bone-Inspired Mineralization with Highly Aligned Cellulose Nanofibers as Template". In: *ACS Applied Materials and Interfaces* 11 (45), pp. 42486–42495. ISSN: 19448252. DOI: 10.1021/acsami.9b15234.

Cooper, J.E. (Jan. 2001). "AEROELASTIC RESPONSE". In: *Encyclopedia of Vibration*, pp. 87–97. DOI: 10.1006/RWVB.2001.0125.

Das, Siddhartha and Aloke Kumar (Nov. 2014). "Formation and post-formation dynamics of bacterial biofilm streamers as highly viscous liquid jets". In: *Scientific Reports* 4. ISSN: 20452322. DOI: 10.1038/srep07126.

Davydova, Ekaterina et al. (Feb. 2016). "Design and evaluation of microfluidic devices for two-dimensional spatial separations". In: *Journal of Chromatography A* 1434, pp. 127–135. ISSN: 18733778. DOI: 10.1016/j.chroma.2016.01.003.

Deuerling, Steffi et al. (May 2018). "A Perspective on Bio-Mediated Material Structuring". In: *Advanced Materials* 30 (19). ISSN: 15214095. DOI: 10.1002/adma.201703656.

Drescher, Knut et al. (Mar. 2013). "Biofilm streamers cause catastrophic disruption of flow with consequences for environmental and medical systems". In: *Proceedings of the National Academy of Sciences* 110 (11), pp. 4345–4350. ISSN: 0027-8424. DOI: 10.1073/PNAS.1300321110. URL: https://www.pnas.org/content/110/11/4345https://www.pnas.org/content/110/11/4345.abstract.

Flemming, Hans Curt and Jost Wingender (Sept. 2010). "The biofilm matrix". In: *Nature Reviews Microbiology* 8 (9), pp. 623–633. ISSN: 17401526. DOI: 10.1038/nrmicro2415.

Galié, Serena et al. (May 2018). "Biofilms in the Food Industry: Health Aspects and Control Methods". In: *Frontiers in Microbiology* 0 (MAY), p. 898. ISSN: 1664-302X. DOI: 10.3389/FMICB.2018.00898.

Goldstein, Richard A. and Orkun S. Soyer (May 2008). "Evolution of taxis responses in virtual bacteria: Non-adaptive dynamics". In: *PLoS Computational Biology* 4 (5). ISSN: 1553734X. DOI: 10.1371/journal.pcbi.1000084.

Hassanpourfard, Mahtab et al. (Aug. 2015). "Bacterial floc mediated rapid streamer formation in creeping flows". In: *Scientific Reports* 5. ISSN: 20452322. DOI: 10.1038/srep13070.

Ichikawa, Yoshiyasu, Ken Yamamoto, and Masahiro Motosuke (July 2018). "Three-dimensional flow velocity and wall shear stress distribution measurement on a micropillar-arrayed surface using astigmatism PTV to understand the influence of microstructures on the flow field". In: *Microfluidics and Nanofluidics* 22 (7). ISSN: 16134990. DOI: 10.1007/s10404-018-2095-8.

J., Ferziger and Peric M. (2008). *Numerische Strömungsmechanik*. Springer Berlin Heidelberg. ISBN: 978-3-540-67586-0. DOI: 10.1007/978-3-540-68228-8.

Kanematsu, Hideyuki and Dana M. Barry (2020). "Biofilm Problems and Environments". In: *Formation and Control of Biofilm in Various Environments*. Singapore: Springer Singapore, pp. 173–200. ISBN: 978-981-15-2240-6. DOI: 10.1007/978-981-15-2240-6_8. URL: https://doi.org/10.1007/978-981-15-2240-6_8.

Klotz, Moritz et al. (2021). "Grow with the flow - mineralised textiles from rheotactic patterned bacterial cellulose".

Kondo, Tetsuo and Wakako Kasai (Oct. 2014). "Autonomous bottom-up fabrication of three-dimensional nano/microcellulose honeycomb structures, directed by bacterial nanobuilder". In: *Journal of Bioscience and Bioengineering* 118 (4), pp. 482–487. ISSN: 13474421. DOI: 10.1016/j.jbiosc.2014.04.002.

Lecheler, Stefan (2014). *Numerische Strömungsberechnung*. Springer Fachmedien Wiesbaden. ISBN: 978-3-658-05200-3. DOI: 10.1007/978-3-658-05201-0.

Lee, Minhyung et al. (2020). "Improvement of Grid Independence Test for Computational Fluid Dynamics Model of Building Based on Grid Resolution". In: DOI: 10.1155/2020/8827936. URL: https://doi.org/10.1155/2020/8827936.

Liu, Hong and Peiwen Li (Apr. 2013). "Even distribution/dividing of single-phase fluids by symmetric bifurcation of flow channels". In: *International Journal of Heat and Fluid Flow* 40, pp. 165–179. ISSN: 0142727X. DOI: 10.1016/j.ijheatfluidflow.2013.01.011.

Liu, Hong, Peiwen Li, and Jon Van Lew (Sept. 2010). "CFD study on flow distribution uniformity in fuel distributors having multiple structural bifurcations of flow channels". In: *International Journal of Hydrogen Energy* 35 (17), pp. 9186–9198. ISSN: 03603199. DOI: 10.1016/j.ijhydene.2010.06.043.

Liu, Miao et al. (July 2017). "Oriented bacterial cellulose-glass fiber nanocomposites with enhanced tensile strength through electric field". In: *Fibers and Polymers* 18 (7), pp. 1408–1412. ISSN: 12299197. DOI: 10.1007/s12221-017-1232-4.

Ma, Jingyun, Yachen Wang, and Jing Liu (Aug. 2017). "Biomaterials meet microfluidics: from synthesis technologies to biological applications". In: *Micromachines* 8 (8). ISSN: 2072666X. DOI: 10.3390/mi8080255.

Marcos et al. (Mar. 2012). "Bacterial rheotaxis". In: *Proceedings of the National Academy of Sciences* 109 (13), pp. 4780–4785. ISSN: 0027-8424. DOI: 10.1073/PNAS.1120955109. URL: https://www.pnas.org/content/109/13/4780https://www.pnas.org/content/109/13/4780.abstract.

Marty, Aurélie et al. (July 2012). "Formation of bacterial streamers during filtration in microfluidic systems". In: *Biofouling* 28 (6), pp. 551–562. DOI: 10.1080/08927014.2012.695351.

Menon, E. Shashi (Jan. 2015). "Fluid Flow in Pipes". In: *Transmission Pipeline Calculations and Simulations Manual*, pp. 149–234. DOI: 10.1016/B978-1-85617-830-3.00005-5.

Muhammad, Musa Hassan et al. (2020). "Beyond Risk: Bacterial Biofilms and Their Regulating Approaches". In: *Frontiers in Microbiology* 11, p. 928. ISSN: 1664-302X. DOI: 10.3389/fmicb.2020.00928. URL: https://www.frontiersin.org/article/10.3389/fmicb.2020.00928.

Oberkampf, William L and Timothy G Trucano (2002). *Verification and validation in computational fluid dynamics*, pp. 209–272.

P, Stoodley et al. (Dec. 2002). "Biofilm material properties as related to shear-induced deformation and detachment phenomena". In: *Journal of industrial microbiology biotechnology* 29 (6), pp. 361–367. ISSN: 1367-5435. DOI: 10.1038/SJ.JIM.7000282. URL: https://pubmed.ncbi.nlm.nih.gov/12483479/.

Pal, Arundhati and · A K Paul (2008). *Microbial extracellular polymeric substances: central elements in heavy metal bioremediation*, pp. 49–64.

P.Rafferty, John. *Beer's law | Definition, Equation, Facts | Britannica*. URL: https://www.britannica.com/science/Beers-law.

Qi, Yipin et al. (Aug. 2019). "Bioinspired Mineralization with Hydroxyapatite and Hierarchical Naturally Aligned Nanofibrillar Cellulose". In: *ACS Applied Materials and Interfaces* 11 (31), pp. 27598–27604. ISSN: 19448252. DOI: 10.1021/acsami.9b09443.

Rusconi, Roberto et al. (Sept. 2010). "Laminar flow around corners triggers the formation of biofilm streamers". In: *Journal of the Royal Society Interface* 7 (50), pp. 1293–1299. ISSN: 17425662. DOI: 10.1098/rsif.2010.0096.

Rusconi, Roberto et al. (Mar. 2011). "Secondary flow as a mechanism for the formation of biofilm streamers". In: *Biophysical Journal* 100 (6), pp. 1392–1399. ISSN: 15420086. DOI: 10.1016/j.bpj.2011.01.065.

Saxena, Shivanjali and Rakesh Joshi (2020). *Microfluidic Devices: Applications and Role of Surface Wettability in Its Fabrication*. URL: www.intechopen.com.

Secchi, Eleonora et al. (2019). "The effect of flow on swimming bacteria controls the initial colonization of curved surfaces". In: *bioRxiv*. ISSN: 2692-8205. DOI: 10.1101/866491.

Sforza, Pasquale (2014). "Chapter 9 - Drag Estimation". In: *Commercial Airplane Design Principles*. Ed. by Pasquale Sforza. Boston: Butterworth-Heinemann, pp. 349–404. ISBN: 978-0-12-419953-8. DOI: https://doi.org/10.1016/B978-0-12-419953-8.00009-7. URL: https://www.sciencedirect.com/science/article/pii/B9780124199538000097.

Sonin, Ain A (2001). *The Physical Basis of DIMENSIONAL ANALYSIS*.

Spiesz, Ewa M. et al. (May 2019). "Bacterially Produced, Nacre-Inspired Composite Materials". In: *Small* 15 (22). ISSN: 16136829. DOI: 10.1002/smll.201805312.

Stoodley, P et al. (2007). "Biofouling The Journal of Bioadhesion and Biofilm Research Flowing biofilms as a transport mechanism for biomass through porous media under laminar and turbulent conditions in a laboratory reactor system Flowing biofilms as a transport mechanism for biomass through porous media under laminar and turbulent conditions in a laboratory reactor system". In: ISSN: 1029-2454. DOI: 10.1080/08927010500375524. URL: https://www.tandfonline.com/action/journalInformation?journalCode=gbif20.

Stoodley, Paul et al. (1998). "Oscillation characteristics of biofilm streamers in turbulent flowing water as related to drag and pressure drop." In: *Biotechnology and bioengineering* 57 5, pp. 536–44.

Sunden, B. (Aug. 2008). "TUBES, CROSSFLOW OVER". In: *A-to-Z Guide to Thermodynamics, Heat and Mass Transfer, and Fluids Engineering*. DOI: 10.1615/ATOZ.T.TUBES_CROSSFLOW_OVER.

Thomen, Philippe et al. (Apr. 2017). "Bacterial biofilm under flow: First a physical struggle to stay, then a matter of breathing". In: *PLoS ONE* 12 (4). ISSN: 19326203. DOI: 10.1371/journal.pone.0175197.

Valiei, Amin et al. (Dec. 2012). "A web of streamers: Biofilm formation in a porous microfluidic device". In: *Lab on a Chip* 12 (24), pp. 5133–5137. ISSN: 14730189. DOI: 10.1039/c2lc40815e.

Vasudevan, Ranganathan (June 2014). "Biofilms: Microbial Cities of Scientific Significance". In: *Journal of Microbiology Experimentation* 1 (3). DOI: 10.15406/JMEN.2014.01.00014.

Versteeg, H K and W Malalasekera (2006). "An Introduction to Computational Fluid Dynamics Second Edition". In: URL: www.pearsoned.co.uk/versteeg.

Vestby, Lene K. et al. (Feb. 2020). "Bacterial Biofilm and its Role in the Pathogenesis of Disease". In: *Antibiotics* 9 (2). DOI: 10.3390/ANTIBIOTICS9020059. URL: /pmc/articles/PMC7167820//pmc/articles/PMC7167820/?report=abstracthttps://www.ncbi.nlm.nih.gov/pmc/articles/PMC7167820/.

Wei, Min et al. (Aug. 2015). "CFD-based evolutionary algorithm for the realization of target fluid flow distribution among parallel channels". In: *Chemical Engineering Research and Design* 100, pp. 341–352. ISSN: 02638762. DOI: 10.1016/j.cherd.2015.05.031.

Weibel, Douglas B. and George M. Whitesides (Dec. 2006). "Applications of microfluidics in chemical biology". In: *Current Opinion in Chemical Biology* 10 (6), pp. 584–591. ISSN: 13675931. DOI: 10.1016/j.cbpa.2006.10.016.

Weng, L et al. (2016). "Development of a Single Cell Trapping Microfluidic Device". In:

Zhuang, X. R. et al. (Oct. 2019). "CFD and experimental analyses of flow distribution uniformity in minichannel reactors with a bifurcation structure manifold". In: vol. 354. Institute of Physics Publishing. DOI: 10.1088/1755-1315/354/1/012045.